Search for cosmic neutrino emission from Milagro sources with ANTARES

Der Naturwissenschaftlichen Fakultät
der Friedrich-Alexander-Universität Erlangen-Nürnberg
zur Erlangung des Doktorgrades Dr. rer. nat.

vorgelegt von
Stefanie Lucia Wagner
aus Forchheim

Als Dissertation genehmigt
von der Naturwissenschaftlichen Fakultät
der Friedrich-Alexander-Universität Erlangen-Nürnberg

Tag der mündlichen Prüfung:	06. Mai 2015
Vorsitzender des Promotionsorgans:	Prof. Dr. Jörn Wilms
Gutachter/in:	Prof. Dr. Ulrich Katz
	Prof. Dr. Gisela Anton

Zusammenfassung

Im Jahr 2013 wies das IceCube Experiment erstmalig kosmische Neutrinoemission nach, indem kaskadenartige hochenergetische Neutrinoereignisse gemessen wurden [1]. Kosmische Neutrinos werden unter anderem erzeugt, wenn Protonen, aus welchen die kosmische Strahlung bei Energien oberhalb von 100 GeV hauptsächlich besteht, mit Photonen, Protonen oder anderen Kernen wechselwirken und dabei Kaonen oder Pionen erzeugen. Neutrale Pionen zerfallen zu Gammaquanten, geladene hingegen zerfallen in Myonen und Myon-Neutrinos. Die Myonen können weiter zerfallen und so entstehen Neutrinos. Gammastrahlung kann auch in elektromagnetischen Prozessen, wie dem inversen Compton-Effekt oder Bremsstrahlung, erzeugt werden, wohingegen Neutrinos nur in hadronischen Wechselwirkungsprozessen erzeugt werden können. Daher könnte die parallele Messung von Gammastrahlung und Neutrinos von den selben Quellkandidaten die Fragen nach den unbekannten Quellen kosmischer Strahlung und nach der Zusammensetzung und der Natur leptonischer und hadronischer Prozesse innerhalb kosmischer Beschleuniger lösen. Mögliche Neutrino Quellkandidaten können in zwei Gruppen eingeteilt werden: galaktische Quellen, z.B. Supernovaüberreste (SNRs), und extra-galaktische Quellen, z.B. Gammastrahlungsblitze (GRBs). Milagro detektierte Gammastrahlungsemission von mehreren galaktischen Quellen, sogenannte PeVatrons, von denen man annimmt, sie würden kosmische Teilchen bis zu Energien von mehreren PeV beschleunigen. Einige von diesen Quellen liegen in der Cygnus Sternenbildungsregion, die ein Bereich mit hoher Sternbildungs- und Sternsterberate ist. Solche Regionen weisen eine hohe Dichte sowohl an molekularen Wolken als auch Supernovaüberresten auf. Wegen der hohen molekularen Dichte der Wolken steigt die Wahrscheinlichkeit einer Wechselwirkung von Protonen, die von SNRs erzeugt und beschleunigt wurden, mit den Atomen der Wolke und somit steigt die Wahrscheinlichkeit für Neutrinoemission im Vergleich zu weniger dichten Regionen. Eine Untermenge der acht mit Milagro gemessenen galaktischen TeV-Gammastrahlungsquellkandidaten ([2],[3]) wurde in [4] untersucht, mit der Vorhersage Neutrinos von diesen Quellen innerhalb von einigen Jahren Datennahme mit dem IceCube Detektor nachweisen zu können. Die Milagro Quellen MGRO J2019+37, MGRO J2031+41, MGRO J1908+06, C1 und C2 sind auch mit dem ANTARES Detektor sichtbar und wurden in dieser Arbeit für die Untersuchung von punktförmiger Neutrinoemission mit ANTARES ausgewählt.

Der ANTARES Detektor, der für den Nachweis von Neutrinos mit Energien im GeV bis in den PeV Bereich optimiert wurde, befindet sich im Mittelmeer und besteht aus 885 optischen Modulen (OMs), die an insgesamt 12 vertikalen Strukturen, sogenannten Lines, installiert sind. Die Lines sind 480 m hoch und sind in einem Abstand von 60 bis 70 m am Meeresboden in einer Tiefe von ca. 2.5 km verankert. Da Neutrinos neutral geladen sind und nur schwach mit Materie wechselwirken, benötigt man ein großes Detektionsvolumen, welches von der Energie der zu untersuchenden Neutrinos sowie vom Fluss derselben abhängt. Der ANTARES Detektor instrumentiert ein Volumen von 0,01 km^3 in der Tiefsee. Ein indirektes Nachweisprinzip wird genutzt, da Neutrinos nur über die schwache Wechselwirkung mit Atomen oder Molekülen inter-

agieren können und dabei hochenergetische Leptonen in geladenen Stromreaktionen erzeugen. Der Fokus liegt hier auf Myon-Neutrinos, die in der geladenen Stromreaktion wechselwirken, da für eine Punkquellenanalyse die gute Winkelauflösung der langen Spur im Detektor nötig ist, welche die erzeugten Myonen erfüllen. Diese relativistischen Teilchen erzeugen Licht über den Cherenkov-Effekt indem sie sich schneller als Licht in dem transparenten Medium Wasser bewegen. Das transmittierte Licht formt einen Lichtkegel unter einem typischen Winkel von $\Theta_c = 42°$ für Wasser. Indem man die Position und die Ankunftszeit der Photonen, die mit den OMs detektiert wurden (=Hits), bestimmt, ist es möglich die Spur der erzeugten Myonen und damit der Neutrinos zu rekonstruieren, da der Zwischenwinkel zwischen Myonen und Neutrinos für Energien oberhalb von mehreren TeV vernachlässigbar ist.

Eine neue Myonen-Spurrekonstruktionsmethode wurde in dieser Arbeit entwickelt um alternative bzw. zusätzliche Ereignisinformationen im Vergleich zu den verwendeten Standardalgorithmen zu bekommen. Die Strategie besteht aus einer Hit-Selektion, einem vorläufigen Fit (Pre-Fit), einen Haupt-Fit und Qualitätsschnitten. Der Pre-Fit basiert auf einer Abrasterung des kompletten Himmels in diskreten Winkelschritten. Indem jede untersuchte Richtung festgehalten wird, muss nur noch die Position der Spur mit einer linearen Anpassung gefunden werden. Für jede Richtung wird eine eigene Hit-Selektion durchgeführt, die eine Kausalitätsbeziehung zwischen Hit-Paaren benutzt. Direkte Signal-Hits müssen vorselektiert werden, da optischer Untergrund, der durch den Zerfall von im Meereswasser vorhandenem ^{40}K oder durch lichtemittierende Fauna (Biolumineszenz) erzeugt wird, im Detektor zufällig verteilt ist und gestreute Signal-Hits, die von der Kegelform abweichen, das Verhalten des Fits beeinflussen können. Jede gefittete Richtung am Himmel bekommt ihre eigenen Qualitätswert, der auf χ^2 und der Anzahl an Hits, die in der linearen Fit Prozedur verwendet wurden, basiert. Die zehn Spurhypothesen mit den höchsten Qualitätswerten werden als Basis für weitere Selektionskriterien verwendet. Zunächst werden Spuren die offensichtlich das Hit-Muster nicht gut beschreiben, ausgefiltert. Das dafür verwendete Kriterium ist das sogenannte Zylinderkriterium, wobei ein Zylinder um die Spur gelegt wird, der alle Hits mit geringen Zeitresiduen (um gestreute Hits zu unterdrücken) enthält. Falls das Verhältnis von Zylinderradius r zu Zylinderhöhe h größer als 1 ist, wird die Spur ausgefiltert. Diese Prozedur ist sehr effizient: ungefähr 80% der rekonstruierten Spuren mit Winkelfehlern größer als 60° werden ausgefiltert, wobei auf der anderen Seite 98,8% der rekonstruierten Spuren mit Winkelfehlern kleiner als 5° behalten werden. Aus der Untermenge an Spuren, die das Zylinderkriterium erfüllen, wird nun eine Spur ausgewählt, die ein Oberflächendichtekriterium der Hits um die Spur am besten erfüllt. Um eine bessere Auflösung zu erhalten wird zudem ein sogenannter MEstimator-Fit benutzt, welcher den Einfluss von Hits mit großen Zeitresiduen unterdrückt. Der Haupt-Fit basiert auf der Methode der maximalen Wahrscheinlichkeit (Maximum-Likelihood), welche die Wahrscheinlichkeitsdichtefunktion (PDF) der Zeitresiduen der Hits verwendet und maximiert. Der Qualitätsparameter, welchen diese Methode zu Verfügung stellt, ist der reduzierte Logarithmus der Wahrscheinlichkeit, kurz rlogL, der sich berechnet als der Logarithmus der Wahrscheinlichkeit geteilt durch die Anzahl an Freiheitsgraden. Hierauf sind Schnitte möglich, je kleiner der rlogL-Wert ist, desto besser ist das Fit-Ergebnis. Die komplette Fit-Prozedur wird KrakeFit genannt.

Mögliche Qualitätsschnittparameter wurden abgeleitet um nur gut rekonstruierte Ereignisse auszuwählen und zusätzlich den atmosphärischen Myonenuntergrund für fälschlicherweise als von unten kommend rekonstruierte atmosphärische Myonen zu unterdrücken. Für von oben kommende Ereignisse ist der amtosphärische Myonenuntergrund um einen Faktor von ca. 10^6 größer als für atmosphärische Neutrinos. Das Verhalten von KrakeFit wurde mit den standard ANTARES Spurrekonstruktionen BBFit und AAFit verglichen. Der Median des Winkelfehlers

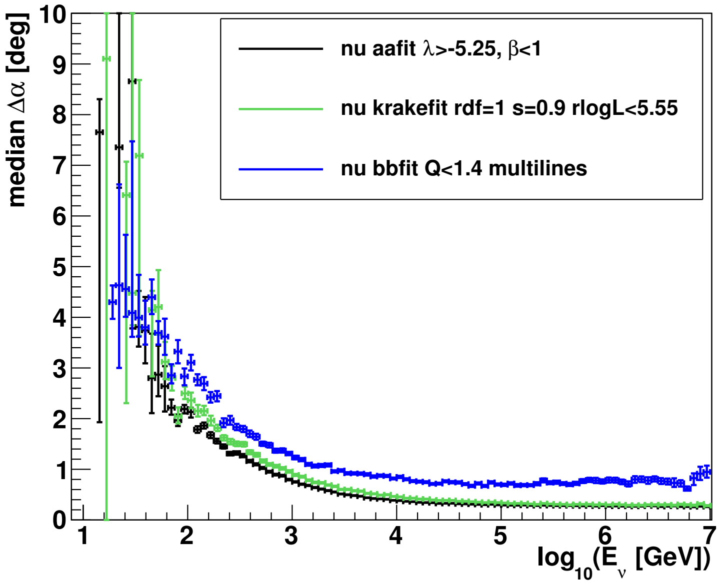

Abbildung 1: Median des Winkelfehlers $\Delta\alpha$ für von unten kommende Neutrinos als Funktion der Neutrinoenergie für AAFit ($\lambda > -5.25$, $\beta < 1°$) (black), BBFit ($Q < 1.4$, NLines > 1) (blue) und KrakeFit (rdf=1, $s > 0.9$, rlogL < 5.55) (green) für ein E^{-2} Spektrum.

in Abhängigkeit von der Energie ist in Abb. 1 gezeigt. BBFit, welches am effizientesten für niederenergetische Neutrinoereignisse ist, hat ein besseres Verhalten als KrakeFit für Ereignisse mit Energien unterhalb von 50 GeV. Für hochenergetische Neutrinoereignisse ist das Verhalten von KrakeFit und AAFit, welches die standard hochauflösende Spurrekonstruktionsstrategie von ANTARES ist, vergleichbar, nachdem Qualitätsschnitte angewendet wurden, die für beide eine vergleichbare Anzahl an falsch rekonstruierten atmosphärischen Myonen ergibt. Ein Vergleich der Ereignisse, die mit KrakeFit und AAFit nach Anwendung von Qualitätsschnitten rekonstruiert wurden, ergibt, dass 35,9% aller getriggerten Ereignisse mit beiden Strategien rekonstruiert werden, 20,8% werden nur mit AAFit rekonstruiert und 5,6% werden zusätzlich mit KrakeFit rekonstruiert. Daher bekommt man durch KrakeFit zusätzliche Neutrinoereignisinformation zu AAFit, was dazu genutzt werden kann um die Neutrinoausbeute zu erhöhen. Der mittlere Zwischenwinkel zwischen den Ergebnissen dieser beiden Spurrekonstruktionen für Ereignisse, die mit beiden als von unten kommend rekonstriert wurden beträgt 1,4°.

KrakeFit ist eine Rekonstruktionsstrategie mit hoher Winkelauflösung - für Neutrinos mit Energien über 1 TeV (10 TeV) ist die Auflösung besser als 0,88° (0,45°) - und einer guten Effizienz für die Rekonstruktion von (hochenergetischen) Neutrinos. Um zu überprüfen ob die Ereignisrekonstruktion arbeitet wie erwartet und ob die Run-für-Run (rbr) basierte Monte Carlo-Simulation (MC) die Daten gut beschreibt wurde ein Daten-MC-Vergleich durchgeführt. Dabei wurden generelle Observablen von KrakeFit wie die Verteilung des Zenit- und Azimut-Winkels, der Anzahl der Hits und Lines, die vom Fit verwendet wurden, für eine Run-Auswahl untersucht. Diese enthält ANTARES Runs, die von 2008 bis 2012 mit der kompletten Detektorkonfiguration aufgezeichnet wurden und einer Lebenszeit von 744,68 Tagen entspricht. Nachdem Qualitätsschnitte angewendet wurden, mit Hauptqualitätsschnitt auf den rlogL-Wert, wurde eine gute Übereinstimmung zwischen Daten und MC beobachtet. Zusätzlich zu den Standard-Observablen wurden weitere Parameter zur Unterscheidung zwischen atmosphärischen Myonen und Neutrinos untersucht. Einige davon sind gute Kandidaten als Schnittparameter. Das sind die Länge der direkten Hits (ausgewählt als Hits mit geringen Zeiresiduen zur rekonstruierten Spur) projeziert auf die Spur, der Sicherheitsparameter des rdf (random decision forest zur Klassifizierung von von unten kommenden und von oben kommenden Myonenspuren) und der Zwischenwinkel zwischen Ereignissen die mit KrakeFit und AAFit rekonstruiert wurden. Da jede Analyse ihre eigenen Anforderungen hat, müssen diese Parameter für jede Analyse separat analysiert und optimiert werden, eventuell auch in einer Kombination von mehreren Parametern.

In dieser Arbeit wird für die Untersuchung der Milagro Quellen die KrakeFit Spurrekonstruktion verwendet. Um den Parameterraum auf eine untersuchbare Anzahl an Parametern zu beschränken werden für die Sensitivitätsstudie einer punktförmigen Neutrinoemission von den Milagro Quellkandidaten nur der rlogL-Wert und ein zusätzlicher Schnitt auf rdf=1 (rdf=1 für von unten kommenden Spuren) untersucht. Die optimalen Schnittwerte wurden für jeden Milagro Quellkandidaten und seiner Neutrinoflussvorhersage im Hinblick eines größtmöglichen Modell-Entdeckungspotentials (MDP) für eine 3σ Entdeckung separat bestimmt. In [4] und [5] wurde die Neutrinoflussvorhersage für MGRO J2019+37, MGRO J2031+41, MGRO J1908+06, C1 und C2 von Messungen des Gammastrahlungsspektrums abgeleitet. Man erwartet, dass dieser einem Potenzgesetz mit exponentiellem Abfall für hohe Energien folgt:

$$\frac{dN_\nu(E_\nu)}{dE_\nu} = k_\nu \left(\frac{E_\nu}{\mathrm{TeV}}\right)^{-\alpha_\nu} \exp\left(-\sqrt{\frac{E_\nu}{E_{cut,\nu}}}\right). \tag{1}$$

Für jede Quelle und Neutrinoflussvorhersage wird eine punktförmige Neutrinosimulation mithilfe der Run-für-Run Simulationsmethode durchgeführt. Da es mehrere CPU-Jahre dauern würde um eine vollständige rbr-Simulation für die Run-Auswahl für eine Quelle durchzuführen wird stattdessen eine kleine Untermenge an Runs verwendet, die definierte Standard-Detektorbedingungen erfüllt und somit den Hauptanteil an Runs repräsentiert. Mit diesen Simulationen wird die Signal Wahrscheinlichkeitsdichtefunktion (PDF) erzeugt, die ein Bestandteil der Maximum-Likelihood-basierten Punktquellenanalysemethode ist. Als Signal PDF S_i wird die Winkelverteilung zur Quellenposition der als von unten kommend rekonstruierten Signal-Ereignisse nach Qualitätsschnitten verwendet. Das ist die sogenannte PSF (point spread function). Als Untergrund PDF B_i wird die Ereignisrate in Abhängigkeit von $\sin(\delta)$ der Deklination δ nach Qualitätsschnitten verwendet. Beide PDFs sind normiert, sodass jeweils ihr Integral über den Raumwinkel 1 ergibt. Eine Maximum-Likelihood-basierte Methode wird gebraucht, da nach Messung einer Spur, die als von unten kommend rekonstruiert wurde, nicht zwischen kosmischen Neutrinos, atmosphärischen Neutrinos und falsch rekonstruierten atmosphärischen Myonen unterschieden werden kann. Deshalb ist ein statistisches Verfahren nötig um zu interpretieren wie signal- oder untergrundartig das Ergebnis ist. Dies wird hier durch einen Hypothesentest gemacht, wobei die Nullhypothese lautet, dass die gemessenen Daten nur aus Untergrundereignissen bestehen. Anstatt die Wahrscheinlichkeit L zu maximieren wird die Teststatistik Q maximiert, welche als

$$\log L(n_s) = \sum_{i=0}^{N} \log\left(\frac{n_s}{N} S_i + \left(1 - \frac{n_s}{N}\right) B_i\right) \tag{2}$$

bzw.

$$Q = \log\left(\frac{\max(L(n_s))}{L(n_s = 0)}\right) = \max(\log L(n_s) - \log L(n_s = 0)) \tag{3}$$

definiert sind, wobei N die Gesamtanzahl an Ereignissen in Daten nach Qualitätsschnitten und n_s die Anzahl an vermuteten Signalereignissen ist. Der Wert μ_s, der der Wert von n_s ist, welcher die Wahrscheinlichkeit bzw. die Teststatistik maximiert, ist die beste Abschätzung für die wahre Anzahl an Signal-Ereignissen. Pseudo-Experimente wurden generiert indem nur Untergrund- bzw. Untergrundereignisse mit vorhandenen Signalereignissen generiert wurden. Das Ergebnis wurde statistisch interpretiert. Anhand der Verteilung von Q für reinen Untergrund wurden die Grenzen von Q für eine 3σ und eine 5σ Entdeckung bestimmt. Es wurde gezeigt, dass der mittlere gefittete Wert von μ_s der Anzahl der injizierten Signal-Ereignisse entspricht und daher der Hypothesentest durchgeführt werden kann. Die besten Schnittwerte (rlogL-Wert mit und ohne rdf=1) wurden optimiert in Hinblick auf das Modell-Entdeckungspotentials (MDP) um die beste Wahrscheinlichkeit einer Entdeckung für die Anzahl der zu erwartenden Ereignisse (die aus der punktförmigen Quellensimulation für jede Quelle und Neutrinoflussvorhersage bestimmt wurden) zu erhalten. Die entsprechende Sensitivität wurde durch Multiplikation des erwartenden Neutrinoflusses mit dem Verhältnis aus der Anzahl der nötigen Ereignisse für eine 50% Chance für eine 3σ Entdeckung $n_{3\sigma}$ und der erwartenden Anzahl an Ereignissen bestimmt. Eine mittlere obere Grenze für 90% C.L. (confidence level) $\bar{\Phi}_{90}$ wurde auf den Neutrinofluss gesetzt. Der Fokus liegt hier bei den Werten, die für die 3σ Optimierung bestimmt wurden, da die Anzahl an erwarteten Neutrinoereignissen in der Größenordnung von 10^{-3} liegt.

Da für die Quellen MGRO J1908+06, MGRO J2019+37 und MGRO J2031+41 mehr als eine Neutrinoflussvorhersage vorhanden ist, werden die finalen Ergebnisse in Tab. 1 für die Neutrinoflüsse und Schnitte mit dem höchsten MDP angegeben. In Abb. 2 werden die Sensitivitäten der fünf Milagro Quellen für eine 3σ Entdeckung gezeigt. Die Sensitivität ist für alle Quellen ungefähr einen Faktor 10^2 höher als der erwartete Neutrinofluss. Es ist daher unwahrscheinlich eine signifikante Anzahl an Neutrinos für eine 3σ Entdeckung zu messen. Das kommt daher, dass die Sichtbarkeit der Quellen im ANTARES Detektor mit einer Sichtbarkeit von 23% bis 30%, außer MGRO J1908+06 mit einer Sichtbarkeit von 48%, klein ist und durch das erwartete Energiespektrum mit exponentiellem Abfall, die meisten Neutrinoereignisse eher niederenergetisch sein werden und damit im atmosphärischen Untergrund verschwinden.

Quelle	Fluss	rlogL	rdf	$n_{3\sigma}$	$\Phi_{3\sigma}$ ($\mathrm{TeV^{-1}cm^{-2}s^{-1}}$)	$\bar{\Phi}_{90}$ ($\mathrm{TeV^{-1}cm^{-2}s^{-1}}$)
MGRO J1908+06	halzen3	5.1	-	1.81	$6.3 \cdot 10^{-10}$	$1.35 \cdot 10^{-9}$
MGRO J2019+37	halzen3	5.2	1	0.93	$3.5 \cdot 10^{-10}$	$9.70 \cdot 10^{-10}$
MGRO J2031+41	kappes	5.3	-	1.07	$8.0 \cdot 10^{-10}$	$2.20 \cdot 10^{-9}$
C1	kappes	5.2	1	1.01	$8.7 \cdot 10^{-10}$	$2.28 \cdot 10^{-9}$
C2	kappes	5.2	1	0.94	$6.3 \cdot 10^{-10}$	$1.76 \cdot 10^{-9}$

Tabelle 1: Zusammenfassung der Neutrinoflussvorhersage und optimierte Schnitte für das beste 3σ Entdeckungspotential pro Quelle. Die Anzahl an nötigen Ereignissen für eine 3σ Entdeckung $n_{3\sigma}$, die Normierung der Sensitiviät $\Phi_{3\sigma}$ und die mittlere obere Grenze für 90% C.L. $\bar{\Phi}_{90}$ sind angegeben.

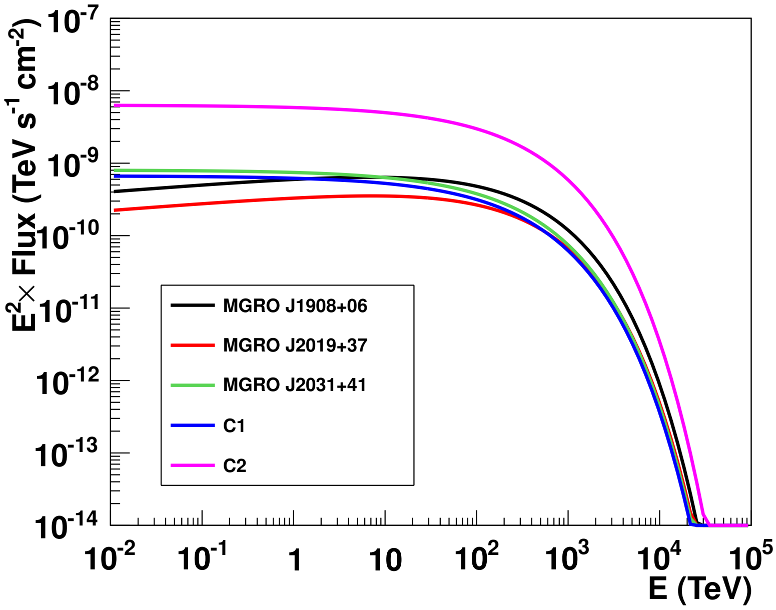

Abbildung 2: Sensitivitäten der fünf Milagro Quellen für eine 3σ Entdeckung für die Neutrinoflussvorhersagen und optimierten Schnitte von Tab. 1.

Für MGRO J1908+06 ist die Neutrinoflussvorhersage, die Sensitivität und die 90% C.L. mittlere obere Grenze, die in dieser Arbeit bestimmt wurden, sowie ein Vergleich zur 90% C.L. oberen Grenze, die mit ANTARES [6] bzw. IceCube [7] für diese Quelle bestimmt wurden in Abb. 3 gezeigt. Die letzteren beiden verwendeten ein E^{-2} Energiespektrum ohne exponentiellem Abfall. Die offizielle ANTARES Analyse berücksichtigt eine größere Run-Auswahl, die einer um das 1,8-fache größeren Lebenszeit als der in dieser Arbeit berücksichtigten entspricht, und das vermutete Neutrinospektrum ohne exponentiellem Abfall ergibt eine höhere Anzahl an erwarteten Neutrinos und daher eine bessere obere Grenze. Es muss erwähnt werden, dass der vermutete E^{-2} Neutrinofluss für diese Quellen nicht physikalisch motiviert ist. Des Weiteren ist der Energiebereich mit den meisten erwarteten Ereignissen mit diesem Fluss nicht angegeben. Der Energiebereich von IceCube für Quellen der nördlichen Hemisphäre wird mit 1 TeV und 1 PeV angegeben. Weder IceCube noch ANTARES konnte mit ihrer neuesten Punktquellenanalyse eine signifikante Anzahl an Neutrinos von MGRO J1908+06 messen.

Um die Auswirkung unterschiedlicher Detektorbedingungen auf die Sensitivität der Quellen systematisch zu untersuchen wurden zusätzliche fünf Detektorbedingungen definiert, wobei in drei von ihnen die Grundlinie der Rate des optischen Untergrunds und in zwei von ihnen die Anzahl an aktiven OMs verändert wurden. Diese Parameter repräsentieren die Arbeits- und Umweltbedingungen des ANTARES Detektors. Mit den simulierten Neutrinoereignissen punktförmiger Neutrinoemission von den fünf Milagro Quellen mit Berücksichtigung dieser Detektorbedingungen wurde die Analyse wiederholt und die Sensitivität für die unterschiedlichen Detektorbedingungen bestimmt. Dies wurde für die Neutrinoflussparametrisierung, die in [4] bestimmt wurde und hier mit kappes bezeichnet wird, da diese für alle fünf Quellen zu Verfügung steht, druchgeführt. Um eine Abschätzung der Unsicherheit auf die Sensitivität für die

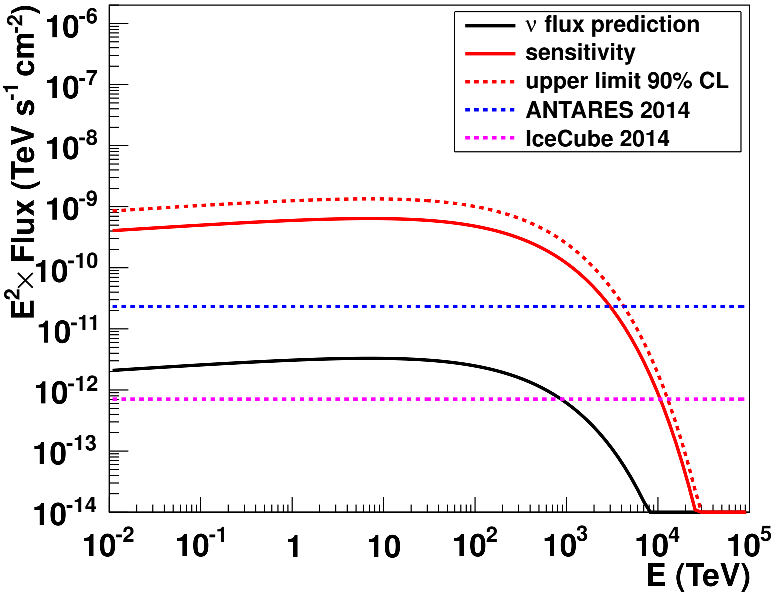

Abbildung 3: Neutrinoflussvorhersage (black), Sensitivität (rote durchgezogene Linie) für eine 3σ Entdeckung und mittlere obere Grenze 90% C.L. (rote gestrichelte Linie) für MGRO J1908+06 für die halzen3 Neutrinoflussvorhersage. Zwei 90% C.L. obere Grenzen für MGRO J1908+06 werden gezeigt, die ein E^{-2} Spektrum ohne exponentiellem Abfall annehmen für ANTARES in blau (bestimmt in [6]) und für IceCube in pink (bestimmt in [7]).

verschiedenen Detektorbedingungen abzuleiten, wurde die Tendenz der Sensitivität jeweils für die Grundlinie der Rate und für die Anzahl an aktiven OMs unabhängig approximiert und ein Intervall um den Median der Verteilung, das 68% der Runs der Run-Auswahl enthält, wurde als Basis für die Fehlerberechnung definiert. Der Fehler auf die Sensitivität wird durch die Anzahl an aktiven OMs mehr beeinflusst als durch die Grundlinie der Rate, da ihre gewählten Werte für die Standard-Detektorbedingungen den Median der Verteilung gut repräsentieren, wohingegen die Verteilung der Anzahl der aktiven OMs breiter ist. Die Sensitivität der Quellen für die kappes Neutrinoflusserwartung konnte für jede Quelle mit Unsicherheit zu

- MGRO J1908+06: $\Phi_{3\sigma} = 9.72^{+10.75}_{-2.41} \cdot 10^{-10}\,\mathrm{TeV}^{-1}\mathrm{cm}^{-2}\mathrm{s}^{-1}$
- MGRO J2019+37: $\Phi_{3\sigma} = 9.60^{+13.06}_{-3.79} \cdot 10^{-10}\,\mathrm{TeV}^{-1}\mathrm{cm}^{-2}\mathrm{s}^{-1}$
- MGRO J2031+41: $\Phi_{3\sigma} = 8.03^{+12.01}_{-4.85} \cdot 10^{-10}\,\mathrm{TeV}^{-1}\mathrm{cm}^{-2}\mathrm{s}^{-1}$
- C1: $\Phi_{3\sigma} = 9.15^{+12.22}_{-4.38} \cdot 10^{-10}\,\mathrm{TeV}^{-1}\mathrm{cm}^{-2}\mathrm{s}^{-1}$
- C2: $\Phi_{3\sigma} = 6.68^{+8.68}_{-2.39} \cdot 10^{-10}\,\mathrm{TeV}^{-1}\mathrm{cm}^{-2}\mathrm{s}^{-1}$

bestimmt werden. Die relativen Fehler sind mit einer mittleren relativen oberen Unsicherheit von 131% und einer unteren Unsicherheit von 41% ziemlich groß. Deshalb ist es unabdingbar eine bessere Run-Auswahl für die rbr-Simulation punktförmiger Neutrinoquellen zu wählen oder die volle rbr-Simulation, welche mehrere CPU-Jahre pro Qulle dauert und damit sehr zeitaufwändig ist, durchzuführen bevor die Daten angesehen werden. Da die Anzahl an erwartenden Ereignissen in der Größenordnung 10^{-3} liegt und die Sensitivität für diese Quellen einen Faktor 10^2 größer als der erwartete Neutrinofluss ist, ist es unwahrscheinlich eine signifikante Anzahl an Neutrinos von diesen Quellen für eine 3σ Entdeckung zu messen. Um zukünftige Analysen nicht mit einem Trialfactor zu belegen werden die Daten nicht angesehen. In der Zukunft könnte man untersuchen, ob eine andere Kombination zusätzlicher oder anderer Schnittparameter, die bereits oben erwähnt wurden, bessere Ergebnisse liefern können. Es wäre sinnvoll eine energieabhängige Komponente in der Signal PDF aufzunehmen, welches die Anzahl an nötigen Ereignissen reduziert [8] und dieses vielleicht mit einer Stacking-Analyse-Methode kombinieren. Zusätzlich kann die Information von KrakeFit durch hinzugefügte Ereignisse, die mit AAFit rekonstruiert werden, erweitert werden, um die Anzahl an Neutrinoereignissen zu erhöhen. Diese Bemühungen könnten zu einer besseren oberen Grenze im Bereich der Neutrinoflussvorhersage führen, aber es wird mit einer hohen Wahrscheinlichkeit nicht zu einer Entdeckung von Neutrinoemission von diesen Quellen mit ANTARES führen.

In dieser Arbeit wurde gezeigt, dass ANTARES nicht in der Lage ist einen physikalisch motivierten Neutrinofluss, der aus Gammastrahlungsmessungen dieser Quellen abgeleitet wurde, und besser motiviert ist als ein generisches E^{-2} Energiespektrum nachzuweisen oder einzugrenzen. Durch Anpassung der Methode, die in dieser Arbeit benutzt wurde, ist es eventuell möglich die obere Grenze auf den Neutrinofluss zu verbessern, jedoch ist ein Nachweis der Quellen mit dem gewählten Modell mit ANTARES unwahrscheinlich.

Contents

Chapter 1

Summary

In 2013 the IceCube experiment found the first evidence for cosmic neutrino emission by detecting cascade-like high-energy neutrino events [1]. Cosmic neutrinos are produced - amongst other mechanisms - when protons, of which cosmic rays with energies above 100 GeV mainly consists, interact with photons, protons or other nuclei and produce kaons or pions. Neutral pions decay to gamma rays, charged pions decay to muons and muon-neutrinos. The muons can decay further so that again neutrinos are produced. Gamma rays can be produced also in electromagnetic processes, such as inverse Compton scattering or Bremsstrahlung, neutrinos can only be produced in the hadronic interaction process. Therefore, measuring gamma rays and neutrinos from the same source candidates could solve the questions of the unknown sources of cosmic rays and of the composition and nature of leptonic and hadronic processes within cosmic accelerators. Possible neutrino source candidates can be divided into two groups: galactic sources, for example supernova remnants (SNRs), and extragalactic sources, for example gamma ray bursts (GRBs). Milagro detected gamma ray emission from several galactic sources, so-called PeVatrons, as they are expected to accelerate cosmic particles up to several PeV. Some of these sources are located in the Cygnus star-forming region, which is a region where the star formation rate and the star death rate is high. Such regions exhibit a high density both of molecular clouds and of SNRs. Because of the higher molecular density of the molecular cloud, the probability for the interaction of protons, accelerated and ejected by the SNRs, with the atoms of the cloud is enlarged and therefore the probability of neutrino emission is enlarged compared to less dense media. A subsample of the eight galactic TeV gamma ray candidate sources measured with Milagro ([2],[3]) was studied in [4], where it is stated that neutrinos from these sources might be detected within several years of data taking with the IceCube neutrino telescope. The Milagro sources MGRO J2019+37, MGRO J2031+41, MGRO J1908+06, C1 and C2 are also observable with the ANTARES detector and are selected for the study of point-like neutrino emission with ANTARES in this thesis.

The ANTARES detector, which is optimized to detect neutrinos from the GeV up to the PeV range is located in the Mediterranean Sea and consists of 885 optical modules (OMs) placed at 12 vertical structures, so-called lines. The lines are 480 m high and are anchored with a distance of 60 to 70 m at the seabed in a depth of about 2.5 km. As neutrinos are neutrally charged and weakly interacting with matter, a large detection volume is necessary depending on the energy of the studied neutrinos and the neutrino flux. The ANTARES detector instruments a volume of 0.01 km^3 in the deep sea. An indirect detection principle is used as neutrinos can interact only in the weak-interaction processes with atoms or molecules producing highly energetic leptons in the charged-current interaction process. Here we focus on the muon-neutrino charged-current

channel as for a point source analysis the good angular resolution of long trajectories within the detector is necessary. The produced muons have this property. These relativistic particles generate light via the Cherenkov-effect by moving faster than light in the transparent medium water. The transmitted light forms a light-cone under a typical angle $\Theta_c = 42°$. Knowing the positions and the arrival time of photons detected by the OMs, it is possible to reconstruct the trajectory, or track, of the produced muon and therefore the produced neutrino as the space angle between them is negligible for neutrino energies above several TeV.

A new muon track reconstruction strategy has been developed in this thesis to obtain alternative or additional event information with respect to the standard algorithms. The strategy consists in a hit selection, prefit, main fit and quality cuts. The prefit is based on a scan of the whole sky in discrete angular steps. Taking each probed direction fixed, only the position of the track has to be fitted with a linear fit. For each direction an hit selection is performed using a causality criterion between hit pairs. Direct signal hits have to be preselected as optical background hits, which are caused by the decay of ^{40}K present in seawater or light emitting fauna (bioluminescence), are randomly distributed within the detector, and scattered signal hits, that deviate from the cone form, can influence the performance of the fit. Each fitted direction at the sky gets its quality value, based on the χ^2 and the number of hits used in the linear fit procedure. The ten track assumptions with the highest quality values are taken as basis for further selection criteria. Firstly, tracks that obviously do not fit the hit sample well are filtered out. The criterion used for this decision is the so-called cylinder criteria, where a cylinder around the track is calculated including all hits with low time residuals to suppress scattered hits. If the fraction of the radius r to the height h of the cylinder has a relation greater than 1, the track is filtered out. This procedure is very efficient: about 80% of tracks reconstructed with angular errors greater then 60° are filtered out, where on the other hand 98.8% of tracks reconstructed with angular errors lower then 5° are kept. With the subsample of fits fulfilling the cylinder criteria only one track is selected based on the surface density of hits around the track. To get better precision an MEstimator fit suppressing hits with large time residuals is used. The final fit is based on a maximum likelihood method using the probability density function of the time residuals of the hits. The quality parameter given by that procedure is the reduced log likelihood value, short rlogL, which is the logarithm of the likelihood divided by the number degrees of freedom. This can be used as cut parameter, the lower the rlogL, the better is the fit result. The whole fitting procedure is called KrakeFit.

In order to select only well reconstructed events and additionally to suppress the background of falsely as upgoing reconstructed atmospheric muons, possible quality cut parameters are derived for KrakeFit. The background of atmospheric muons is about a factor 10^6 higher than the number of atmospheric neutrinos for downgoing events. The performance of KrakeFit is compared to the standard ANTARES track reconstruction strategies BBFit and AAFit. The median angular error depending on the energy is shown in Fig. 1.1. BBFit, which is most efficient for low-energetic neutrino events, has a better performance than KrakeFit for energies below 50 GeV. For high-energy neutrino events, the performance of KrakeFit and AAFit, which is the standard high-resolution track reconstruction strategy of ANTARES, are comparable after applying cuts for which both give comparable numbers of misreconstructed atmospheric muons. A comparison of the events reconstructed with KrakeFit and AAFit, applying quality cuts, gives that 35.9% of all triggered events were reconstructed with both strategies, 20.8% were only reconstructed with AAFit and 5.6% were additionally reconstructed with KrakeFit. So KrakeFit gives additional neutrino event information to AAFit and can be used to enhance the amount of neutrinos. The mean of the space angle between the results of the two reconstruction strategies

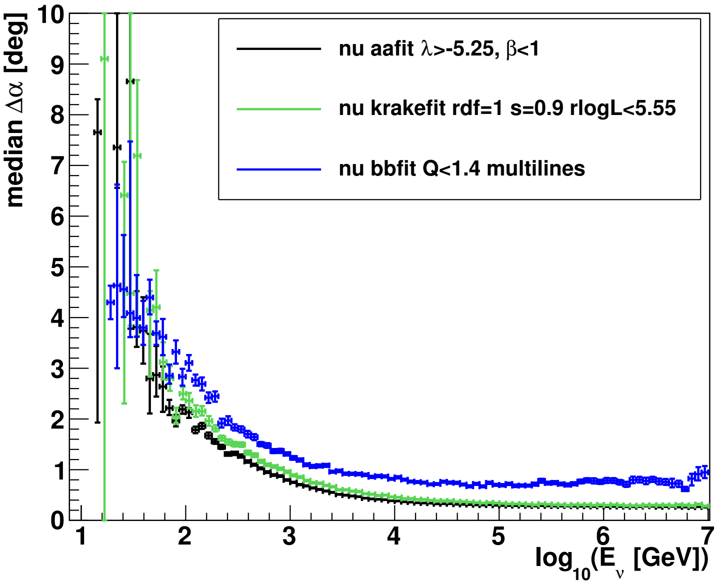

Figure 1.1: Median angular error $\Delta\alpha$ for upgoing neutrino events as a function of the neutrino energy for AAFit ($\lambda > -5.25$, $\beta < 1°$) (black), BBFit ($Q < 1.4$, NLines > 1) (blue) and KrakeFit (rdf=1, $s > 0.9$, rlogL < 5.55) (green) for an E^{-2} energy spectrum.

for events reconstructed with both as upgoing is 1.4°.

KrakeFit is a reconstruction strategy which has a high angular resolution - for neutrinos with energies above 1 TeV (10 TeV) the resolution is better then 0.88° (0.45°) - and a good efficiency for the reconstruction of (high-energy) neutrinos. To inspect if the event reconstruction works as expected and if the run-wise-based (rbr) Monte Carlo simulation (MC) describes the data well, a data-MC-comparison was performed. Here general observables of KrakeFit as the distribution of for example the zenith, azimuth, number of hits and number of lines used in the fit were studied for a run-selection. This includes ANTARES runs that were recorded from 2008 to 2012 with the full-detector configuration and correspond to a live-time of 744.68 days. After applying quality cuts, the main one on the rlogL value, a good agreement between data and MC is observed. In addition to the standard observables further parameters to distinguish between atmospheric muons and neutrinos are studied. Some of them are good candidates for cut parameters. These are the length of direct hits (determined as hits with low time residuals to the fitted track) projected on the track, the safety parameter of the rdf (random decision forest up-down classifier) and the space angle between KrakeFit- and AAFit- reconstructed events. These have to be studied and optimized, maybe also in combination, for each analysis separately as each analysis has different requirements.

The KrakeFit track reconstruction strategy is now applied to a study of the Milagro sources. To limit the parameter space to a feasible number of parameters for the study of the sensitivity of point-like high-energy neutrino emission from the Milagro source candidates, only the rlogL value and an additional cut on the rdf=1 (rdf=1 for upgoing tracks) was studied. The optimal cut values are determined for each Milagro source candidate and their neutrino flux predictions separately with respect to the best MDP (model discovery potential) for a 3σ discovery. In [4] and [5] the neutrino flux predictions of MGRO J2019+37, MGRO J2031+41, MGRO J1908+06, C1 and C2 are derived from measurements of their gamma ray spectrum and is predicted following a power law with exponential cut-off:

$$\frac{dN_\nu(E_\nu)}{dE_\nu} = k_\nu \left(\frac{E_\nu}{\text{TeV}}\right)^{-\alpha_\nu} \exp\left(-\sqrt{\frac{E_\nu}{E_{cut,\nu}}}\right). \tag{1.1}$$

For each source and neutrino flux assumption a point-like neutrino simulation using the rbr simulation scheme was performed. As it takes several CPU-years to produce a rbr simulation for each of the selected runs for one source, a subsample of runs is used instead which fulfil a standard detector condition defined to represent the majority of runs. With these simulations the signal PDF (probability density function) was created, which is one input for the maximum-likelihood-based point source analysis method. As signal PDF S_i the spacing distribution to the source of upgoing reconstructed signal events after applying quality cuts is taken. This is the so-called PSF (point spread function). As background PDF B_i the event rate per $\sin(\delta)$ of declination δ is taken after applying quality cuts. Both are normalized so that the integral over the solid angle for each is equal to 1. A maximum-likelihood-based method is needed as after measuring a trajectory reconstructed as upgoing one cannot distinguish between cosmic neutrinos, atmospheric neutrinos and misreconstructed atmospheric muons. Therefore a statistical approach has to be used to interpret how signal- or respectively background-like the result is. This is done by hypotheses testing where the null hypothesis is that the measured data only consists of background events. The method of maximizing the test statistic Q is used instead of maximizing the likelihood L, which are defined as

$$\log L(n_s) = \sum_{i=0}^{N} \log\left(\frac{n_s}{N} S_i + \left(1 - \frac{n_s}{N}\right) B_i\right) \tag{1.2}$$

and

$$Q = \log\left(\frac{\max(L(n_s))}{L(n_s = 0)}\right) = \max(\log L(n_s) - \log L(n_s = 0)) \tag{1.3}$$

respectively, where N is the total number of events in data after applying quality cuts and n_s is the number of assumed signal events. The value μ_s, which is the value of n_s that maximizes the likelihood or respectively the test statistic, is the best estimate for the true number of signal events. Pseudo-experiments are generated by generating only background and background with present signal event samples. The outcome is interpreted statistically. From the distribution of Q for the background-only distribution the threshold of Q for a 3σ and a 5σ discovery can be determined. It is shown that the mean fitted value of μ_s corresponds to the number of injected events and thus the hypotheses test can be performed. The best cut values (rlogL value with and without rdf=1) are optimized due to the model discovery potential (MDP) to get the best probability for discovery for the expected number of events (determined from the point source simulation per source and neutrino flux assumption). The corresponding sensitivity is determined by multiplying the expected neutrino flux by the factor of the number of events necessary for a 50% chance of a 3σ discovery $n_{3\sigma}$ divided by the number of expected events. An average upper limit for 90% confidence level (C.L.) $\bar{\Phi}_{90}$ on the flux is set. The focus lies on the values determined for 3σ optimization as the number of expected events is in the order of 10^{-3}.

As there are more then one flux assumption per source available for the sources MGRO J1908+06, MGRO J2019+37 and MGRO J2031+41 the final results given in Tab. 1.1 are taken

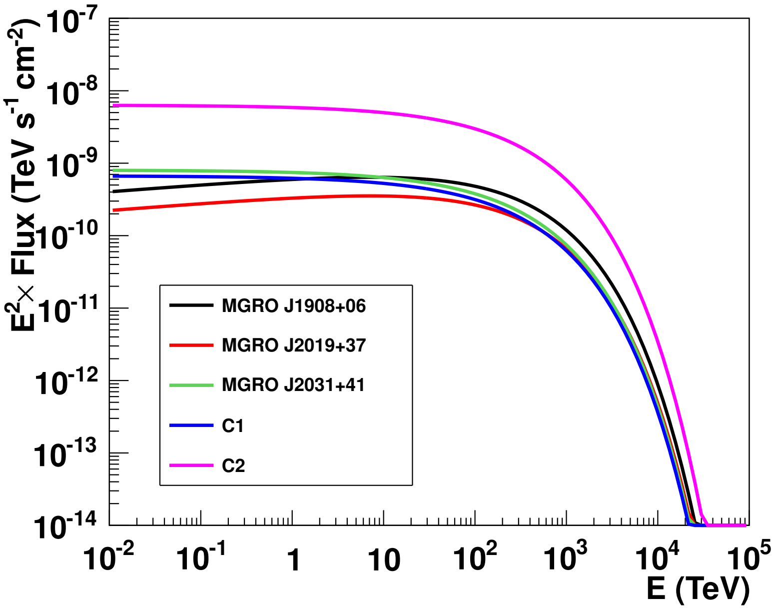

Figure 1.2: Sensitivity of the five Milagro sources for a 3σ discovery for the flux assumptions and optimized cuts given in Tab. 1.1.

from the cuts and neutrino flux assumptions with the highest MDP per source. In Fig. 1.2 the sensitivities for a 3σ discovery for the five Milagro sources is shown. The sensitivity is for all sources about a factor 10^2 higher then their expected neutrino flux. It is unlikely to measure a significant amount of neutrinos for a 3σ discovery. This is caused by the fact that the visibility of these sources within the ANTARES detector is low, it is about 23% to 30%, except for MGRO J1908+06 with a visibility of 48%, and by the fact that the expected energy spectrum has an exponential cut-off, so the neutrino events will be mostly low-energetic and therefore disappear in the atmospheric background.

For MGRO J1908+06 the neutrino flux assumption, the sensitivity and the 90% C.L. average upper limit determined in this thesis is shown in Fig. 1.3 in comparison to the 90% C.L. upper

source	flux	rlogL	rdf	$n_{3\sigma}$	$\Phi_{3\sigma}$ (TeV^{-1}cm^{-2}s^{-1})	$\bar{\Phi}_{90}$ (TeV^{-1}cm^{-2}s^{-1})
MGRO J1908+06	halzen3	5.1	-	1.81	$6.3 \cdot 10^{-10}$	$1.35 \cdot 10^{-9}$
MGRO J2019+37	halzen3	5.2	1	0.93	$3.5 \cdot 10^{-10}$	$9.70 \cdot 10^{-10}$
MGRO J2031+41	kappes	5.3	-	1.07	$8.0 \cdot 10^{-10}$	$2.20 \cdot 10^{-9}$
C1	kappes	5.2	1	1.01	$8.7 \cdot 10^{-10}$	$2.28 \cdot 10^{-9}$
C2	kappes	5.2	1	0.94	$6.3 \cdot 10^{-10}$	$1.76 \cdot 10^{-9}$

Table 1.1: Summary of the flux assumptions and optimized cuts for the best 3σ discovery potential per source. The number of $n_{3\sigma}$, the normalization of the sensitivity $\Phi_{3\sigma}$ and the average upper limit for 90% C.L. $\bar{\Phi}_{90}$ are also shown.

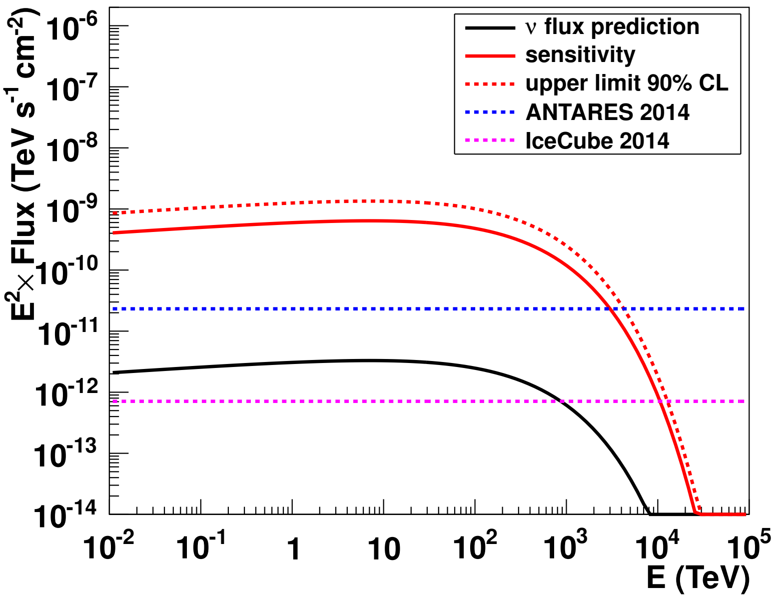

Figure 1.3: Neutrino flux assumption (black), sensitivity (red continuous line) for a 3σ discovery and average upper limit 90% C.L. (red dashed line) for MGRO J1908+06 for the halzen3 neutrino flux assumption. Two 90% C.L. upper limits are shown assuming an E^{-2} energy spectrum without cut-off energy determined for MGRO J1908+06 for ANTARES in blue (derived in [6]) and for IceCube in pink (derived in [7]).

limits determined by ANTARES [6] and IceCube [7] for this source, the latter two assume an E^{-2} energy spectrum without cut-off energy. The official ANTARES analysis considers a larger run selection with a live-time 1.8 times larger than considered in this thesis, and the assumed neutrino flux spectrum without cut-off energy gives an higher amount of expected neutrinos and therefore a better upper limit. It has to be mentioned that the assumed E^{-2} neutrino flux without cut-off is not physically motivated for theses sources. Further the energy range of the majority of events expected from that flux is not stated. The energy range of IceCube for northern hemisphere sources is between 1 TeV and 1 PeV. Neither IceCube nor ANTARES have seen any significant amount of neutrinos from MGRO J1908+06 in their latest point source analysis of this source.

To systematically study the effect of different detector conditions on the sensitivity, additionally five detector conditions are defined where in three of them the baseline rate of the optical background and in two of them the number of active OMs is changed being representatives for the working and environmental conditions of the ANTARES detector. With the simulation of point-like neutrino emission of the five Milagro sources applying these detector conditions and the neutrino flux parametrization of [4], named kappes, as this is available for all five Milagro sources, the analysis was repeated and the sensitivity for these conditions is determined. To derive an estimate of the uncertainty on the sensitivity due to different detector conditions an approximation of the trend of the sensitivity is made for the baseline rate and number of active OMs separately and an interval which contains 68% of all runs around the median of the distributions is taken as basis for the error calculation. The error on the sensitivity is more effected by the number of active OMs than the baseline rate, as the chosen value for standard detector conditions represents the median of the distribution well there, whereas the spread of the number of active OMs is wider. The sensitivity of the sources for the kappes neutrino flux assumption for each source with uncertainties could be determined to

- MGRO J1908+06: $\Phi_{3\sigma} = 9.72^{+10.75}_{-2.41} \cdot 10^{-10}\,\mathrm{TeV}^{-1}\mathrm{cm}^{-2}\mathrm{s}^{-1}$
- MGRO J2019+37: $\Phi_{3\sigma} = 9.60^{+13.06}_{-3.79} \cdot 10^{-10}\,\mathrm{TeV}^{-1}\mathrm{cm}^{-2}\mathrm{s}^{-1}$
- MGRO J2031+41: $\Phi_{3\sigma} = 8.03^{+12.01}_{-4.85} \cdot 10^{-10}\,\mathrm{TeV}^{-1}\mathrm{cm}^{-2}\mathrm{s}^{-1}$
- C1: $\Phi_{3\sigma} = 9.15^{+12.22}_{-4.38} \cdot 10^{-10}\,\mathrm{TeV}^{-1}\mathrm{cm}^{-2}\mathrm{s}^{-1}$
- C2: $\Phi_{3\sigma} = 6.68^{+8.68}_{-2.39} \cdot 10^{-10}\,\mathrm{TeV}^{-1}\mathrm{cm}^{-2}\mathrm{s}^{-1}$.

The relative errors are with a mean relative upper uncertainty of 131% and lower uncertainty of 41% quite high. So it is indispensable to take a better selection of runs for the point-like rbr simulation process or do the fully rbr simulation, which takes several CPU-years per source and is very time consuming, before unblinding the data. As the number of expected events is of the order of 10^{-3} and the sensitivity for these sources is about a factor of 10^2 higher than the expected neutrino flux, it is unlikely to measure a significant amount of neutrinos from these sources for a 3σ discovery with ANTARES. To not constrain further analyses with a trial factor the data are not unblinded. In the future it could be studied if another combination of additional or different cut parameters mentioned above could give better results. It would be useful adding an energy-dependent component in the signal PDF, which was shown to lower the number of necessary events [8] maybe combined with a stacking analysis approach and add to the information of KrakeFit events reconstructed with AAFit to enhance the amount of neutrinos. These efforts could lead to a better upper limit in the area of the neutrino flux prediction, but it won't lead to high probability to a discovery of neutrino emission from these sources with ANTARES.

In this thesis it is shown that ANTARES is not able to detect or constrain physically motivated neutrino flux predictions, derived from gamma ray measurements of these sources, which are better motivated than an E^{-2} energy spectrum. By adjusting the method used in this thesis, the upper limit could be improved, but a detection of these Milagro sources with the selected model with ANTARES is unlikely.

Chapter 2

High-energy neutrino sources

When talking about neutrino astronomy, neutrinos with energies in the range of several GeV up to PeV are studied which are assumed being of cosmic origin. IceCube detected cascade-like neutrino events, which is the first evidence of a diffuse cosmic neutrino flux, but they could not identify point-like neutrino sources up to now [1].

In this thesis cosmic neutrino emission from point-like sources with the ANTARES detector are studied. Therefore high-energy track-like muon-neutrino events are selected and analysed. When talking about high-energy neutrino events, neutrinos with energies above several TeV are meant. In this chapter the purpose of neutrino astronomy is motivated starting with the composition and measured spectrum of cosmic rays. Some potentially cosmic neutrino source candidates are shown grouped in galactic and extragalactic sources. Possible cosmic ray acceleration processes and neutrino flux predictions are described with respect to the candidate source selection of this thesis.

2.1 Cosmic rays

The primary cosmic rays[1] (for energies above 100 GeV) consist of charged particles mainly of hadrons (ionized atoms) and only a tiny amount of electrons [9]. Their composition is splitted into ca. 85% protons, 12% α-particles and ca. 3% heavier nuclei [10]. A lot of experiments measured the cosmic ray composition and fluxes depending on energy in direct measurements like satellite or balloon measurements and for energies above 100 TeV in measurements of their secondary particles in air shower experiments. The flux is summarized in Fig. 2.1. The flux is multiplied with energy to make structures visible. The points where the spectral index γ of the energy spectrum ($dN/dE \propto E^{-\gamma}$) changes are called knee, second knee and ankle. For energies up to the PeV range $\gamma = 2.7$, than it steepens to $\gamma = 3.1$ (knee), and it steepens again at the second knee and flattens again at the ankle [11]. As the cosmic ray flux decreases rapidly with energy huge detectors are necessary to measure a significant amount of them within several years for large energies.

To study the mechanisms of acceleration and learn about the sources of cosmic rays, charged particles are not a good messenger as magnetic fields can deflect them during their flight to Earth. A possible method is using electrically neutral particles as gamma rays and neutrinos.

[1]Primary cosmic rays are particles originally produced by the cosmic ray source, whereas secondary cosmic rays are particles produced by the interaction of primary cosmic rays with molecules or atoms of the interstellar medium or the atmosphere of the Earth.

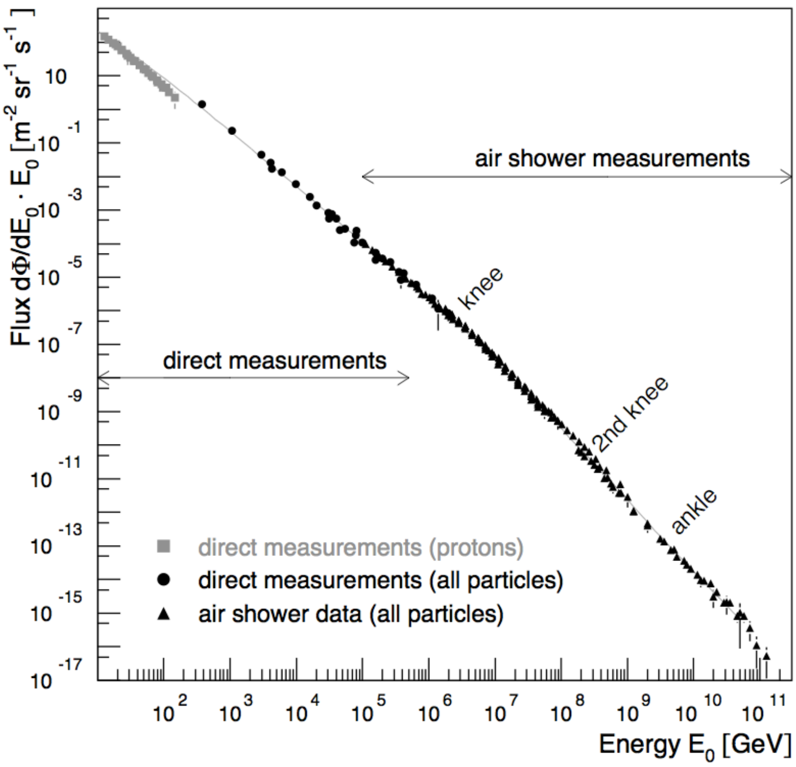

Figure 2.1: Energy spectrum of primary cosmic ray particles measured directly with detectors above the atmosphere and with air shower detectors. Figure taken from [11].

These are produced in a sequence of reactions almost exclusively starting with accelerated cosmic ray protons which can interact with protons, gammas or other nuclei producing hadrons, mostly neutral and charged pions. The neutral pions decay rapidly with a lifetime of $8.4 \cdot 10^{-17}$ s almost exclusively into two gammas [10]

$$\pi^0 \rightarrow \gamma + \gamma. \tag{2.1}$$

The charged pion decays into muons and muon-neutrinos with a lifetime of 26 ns [10]

$$\pi^+ \rightarrow \mu^+ + \nu_\mu, \quad \pi^- \rightarrow \mu^- + \bar{\nu}_\mu. \tag{2.2}$$

In a following process the produced muons can decay to electrons and electron-neutrinos:

$$\mu^+ \rightarrow e^+ + \nu_e + \bar{\nu}_\mu, \quad \mu^- \rightarrow e^- + \bar{\nu}_e + \nu_\mu. \tag{2.3}$$

While gamma rays can also be produced in electromagnetic processes as inverse Compton scattering or Bremsstrahlung, neutrinos can only be produced in the hadronic case. Therefore measuring both neutrinos and gamma rays from cosmic sources solves the problem of the unknown composition of leptonic and hadronic processes of cosmic accelerators. Additionally to their electrically neutral property the small interaction cross-section of neutrinos leads to the fact that they are not absorbed by molecular dust or interstellar media and that they can even pass the Earth without interacting (for energies below 1 PeV). In summary they point back to their sources and can also be emitted from inner parts of the sources which allows to study also inner effects. This nature is used by high-energy neutrino observatories like ANTARES [12] and IceCube [13].

2.2 Cosmic neutrino sources

Possible cosmic neutrino sources can be divided into two groups: galactic sources and extra-galactic sources. A short overview of source candidate classes from both groups are given here. More information about neutrino astronomy and its link to study also particle physics and exotic phenomena is given in the review [9].

2.2.1 Galactic sources

Galactic sources are sources that are located within our galaxy. They are assumed being the primary source for particles with energies up to the knee in the cosmic ray energy spectrum (see Fig. 2.1). The source classes include supernova remnants (SNRs), pulsar wind nebular (PWNs) and star-forming regions.

SNRs are the rest of the stars from supernova explosions. Fermi postulated a mechanism called shock acceleration or first order Fermi acceleration that is assumed to accelerate hadrons in those sources. It is based on the fact that charged particles gain energy by multiple scattering between two shock fronts formed by the ejection from the supernova explosion [10]. Taking this as basis one can derive that the energy spectrum for neutrinos from such sources follows roughly an E^{-2} power law [9].

The class pulsar wind nebula is a special type of supernova remnant, where a pulsar is present and ejecting material in a nebula. The most studied candidate is the crab nebula.

Molecular clouds and magnetic clouds are possible cosmic ray accelerators following Fermi second order acceleration also known as Fermi mechanism [10]. If cosmic ray particles interact with gas clouds moving with a certain velocity $\vec{u}$, they can gain energy by multiple reflection with the cloud. Depending on the relative direction of motion of the particle and the cloud, the particle can gain or loose some energy per reflection process. On average the energy gain is proportional to u^2. As the velocity of such clouds is small, it takes long time for a certain energy gain. Therefore magnetic clouds are assumed being the main collision partners as the interaction probability is larger because of the higher gas density [10].

The detection probability of neutrinos from sources located in regions, where for example a SNR is combined with dense media as molecular clouds, is expected to be enlarged as the probability for particle interaction in such regions (and therefore neutrino production) is higher then in less dense media. This happens for example in so-called star-forming regions, where the star-formation rate is enlarged. 2007 the Milagro experiment measured gamma ray emission from galactic sources, where some of them are located in the Cygnus star-forming region [3]. They are assumed being PeVatrons, accelerators of cosmic rays up to energies of several PeV [14], that produce neutrinos with an energy spectra up to several TeV. Those Milagro sources that can be detected with the ANTARES neutrino telescope have been selected for this study (see chapter 6).

Prediction of neutrino fluxes for galactic sources

As no direct primary cosmic ray measurements are available for the studied sources, neutrino fluxes can be predicted using high-energy photon measurements of the respective sources. This is based on the fact that in hadronic processes neutrino and gamma ray fluxes are correlated as the energy is distributed evenly between the three different types of pions in hadronic collisions [15]. The measured gamma ray flux is transformed using models of pion production in proton-proton collisions and models of their secondary particles to estimate the proton flux of the sources and transformed back to estimate the neutrino fluxes. This is done for example in [16] and [15]. This procedure is complex and underlies various assumptions and uncertainties. If no gamma ray flux measurements and therefore no neutrino flux predictions are available for the source candidates under study, an overall E^{-2} energy spectrum is used motivated by Fermi first order acceleration. Because of this and because of the fact that there are many different theoretical models of the neutrino flux predicted per source and per source class, an overall E^{-2} spectrum is used for comparison purposes and to optimize the direction reconstruction strategies for cosmic neutrinos.

2.2.2 Extragalactic sources

Extragalactic sources are assumed to constitute the primary component of cosmic rays beyond the ankle in the cosmic ray spectrum. Candidate source classes are gamma ray bursts (GRBs), active galactic nuclei (AGNs) and starburst galaxies. The predictions of their neutrino flux show a wider range. They are modeled according to different theoretical models as it is done for GRBs for example in [17].

GRBs are short gamma ray emissions that occur suddenly and without prediction with a duration of seconds (short gamma ray bursts) up to minutes (long gamma ray bursts) [10]. They are studied for example in [17] and [18], but no evidence for neutrinos from such sources could be found with significance.

AGNs consist of a super massive black hole in their center surrounded by a rotating accretion disc which transports material into the center. Perpendicular to the accretion disc jets are formed from particles accelerated near the black hole or the nucleus of a compact galaxy and injected into the radiation field of the source [10]. Shock fronts, formed in the jet, are supposed to accelerate protons and electrons according to Fermi shock acceleration, which initiate hadronic respectively electromagnetic cascades, producing neutrinos and gamma rays according to the processes mentioned above. If a neutrino telescope looks into the direction of the jet, neutrinos from such AGNs could be observed. This is studied in [19] for ANTARES, but no evidence for neutrino emission from these sources could be observed.

Starburst galaxies are galaxies where the rate of star-formation and also death is high. The high rate of supernova explosions in their center leads to a "galactic-scale wind" [9]. According to the fact that supernova remnants are possible neutrino source candidates, as already discussed in the section of galactic sources, this high concentration of supernova explosions and their resulting cosmic ray particle rate together with a high matter density, are good reasons regarding them as possible neutrino sources, which is not studied so far.

There are no dedicated neutrino flux predictions available for starburst galaxies in contrast to the Milagro sources, where the neutrino flux assumption is derived from the measured gamma ray spectrum for each source separately for example in [4] and [5] (as can be seen in section 6.2). Instead of starburst galaxies these sources are located in the galactic plane which is one of the main visible parts of the sky observed by ANTARES. As stated in [4], IceCube might detect neutrinos from these sources with significance within several years of data taking. So a complementary analysis with ANTARES data is useful as this is not done so far. Therefore those Milagro sources visible with ANTARES are chosen for this study.

In the following an overview of the detection principle of high-energy neutrinos with the ANTARES detector is given. Further a new muon track reconstruction algorithm is developed where an overall E^{-2} spectrum is used to optimize the strategy and compare it with other track reconstruction algorithms (see chapter 4). A dedicated data and Monte Carlo simulation (MC) comparison of main reconstruction observables is done in chapter 5 to ensure that the fit works as expected and that the observables of the fit for data are described well by them of the MC. With this new strategy a point-like neutrino source search for the selected Milagro sources is performed using an maximum likelihood-based analysis method (see chapter 7), where the results for the different neutrino flux assumptions per Milagro source are discussed in chapter 8.

Chapter 3

Neutrino detection with the ANTARES detector

Neutrinos can be measured indirectly by their weak interaction products producing light in transparent media like water or ice using the Cherenkov-effect. The technical requirements for using this technique depends on the studied energy range as for example the expected neutrino flux decreases exponentially with energy. Measuring solar neutrinos with energies of several MeV can be done by underground experiments (like Super-Kamiokande [20] or SNO [21]). To measure neutrinos with energies above several GeV up to PeV large scale neutrino detectors are necessary. ANTARES, for example, with an energy threshold of 10 GeV, has an instrumented volume of about $0.01\,\mathrm{km}^3$. Those detectors can only be build in natural water or ice reservoirs as for example the Mediterranean Sea for ANTARES or the South Pole for IceCube. In this chapter the detection principles with the neutrino interaction processes, the Cherenkov-effect and the light propagation are described, where the focus lies on neutrino detectors using water as transparent media as ANTARES data are analysed in this thesis. Further it concentrates on the measurement of muon-neutrinos with energies above 1 TeV producing muons interacting in the charged-current reaction, as those events are regarded for the point source analysis later on. An overview of the ANTARES detector layout and data taking and the influence of environmental conditions are given.

3.1 Detection principle

3.1.1 Neutrino interaction processes

Neutrinos ν_l(or anti-neutrinos $\bar{\nu}_\mathrm{l}$) can only interact via the weak interaction in so-called charged-current or neutral-current interactions with nucleons N by exchanging an Z- or $W^{\pm}$-boson [22]. The following scheme shows these interactions where l is a lepton (e,μ,τ) and X is the hadronic end state.

- Neutral-current reaction (NC):

$$\nu_\mathrm{l} + \mathrm{N} \rightarrow \nu_\mathrm{l} + \mathrm{X} \tag{3.1}$$

$$\bar{\nu}_\mathrm{l} + \mathrm{N} \rightarrow \bar{\nu}_\mathrm{l} + \mathrm{X} \tag{3.2}$$

- Charged-current reaction (CC):

$$\nu_{\rm l} + {\rm N} \rightarrow {\rm l}^- + {\rm X} \tag{3.3}$$

$$\bar{\nu}_{\rm l} + {\rm N} \rightarrow {\rm l}^+ + {\rm X}. \tag{3.4}$$

Both reactions end up in shower events which are studied in detail for example in [23], whose precision of the direction of the shower is not as good as for the produced lepton in the CC-reaction. As for the detection of point-like neutrino sources the neutrino direction has to be known with high precision, this thesis concentrates on the charged-current interaction, which produces high-energy muon events (see section 3.1.4) as for neutrino astronomy purposes the direction of the neutrino has to be known with high precision. The mean space angle β between neutrino and produced muon direction is given by [24]

$$\bar{\beta} = \frac{0.7^\circ}{(E_\nu/\text{TeV})^{0.6}}. \tag{3.5}$$

As the angle between neutrino and lepton direction decreases with neutrino energy, for energies above several TeV it is negligible. Measuring the direction of the lepton, for energies above several TeV, can therefore be used to determine the direction of the initial neutrino.

3.1.2 Cherenkov-effect

The measurement of the direction of this lepton depends on the measurement of the Cherenkov-light produced when charged particles move in a transparent media faster than the light in this media. This effect is known as Cherenkov-effect [25]. The radiation is emitted with an angle Θ_c typical for the transparent media for example water or ice. For the relevant energies $\Theta_c = 42^\circ$ for sea water with an refrective index of $n = 1.35$ and a wavelength of 450 nm [24]. Fig. 3.1 shows a drawing of the emission of Cherenkov-light for a muon produced in a CC-interaction of a muon-neutrino, where the light front forms a cone with opening angle $\gamma = 90^\circ - \Theta_c$. As the light propagation has this geometrical dependency relative to the direction of motion, it is possible to reconstruct the direction of the lepton by measuring the position and arrival time of single photons of the light cone detected at photon detection units, which are illustrated as grey circles in Fig. 3.1.

3.1.3 Propagation of light in seawater

The emitted Cherenkov-light can be scattered or absorbed at the molecules of water or ice. So the intensity of light is reduced by processes which are described by the absorption length $\lambda_{\rm abs}$ and the scattering length $\lambda_{\rm scat}$. These are summarized in the attenuation length $\lambda_{\rm att}$, which is defined as

$$\frac{1}{\lambda_{\rm att}} = \frac{1}{\lambda_{\rm abs}} + \frac{1}{\lambda_{\rm scat}} \tag{3.6}$$

and describes the length where the intensity $I(d)$ is reduced to $1/e$ of the original intensity I_0. The attenuation effect of light in seawater is determined to be smallest in the regime of blue light at wavelengths between 460 nm and 470 nm [26]. The absorption length, determined by a data to Monte Carlo simulation (MC) comparison for data collected in in situ measurements of ANTARES, is in the range between 55 and 65 m [24].

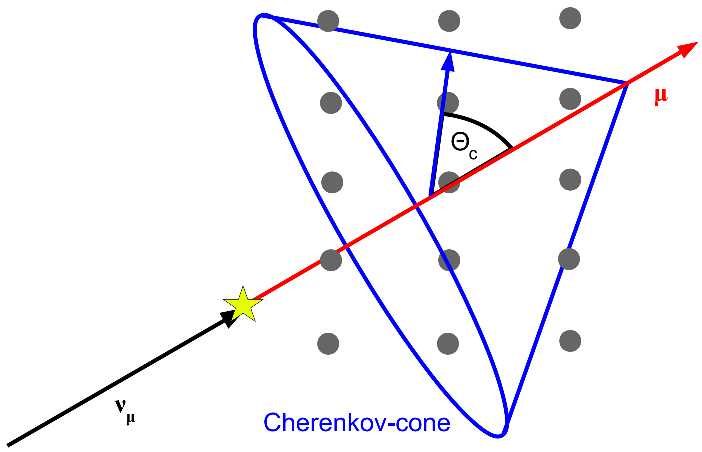

Figure 3.1: Scheme of the Cherenkov-cone shown for a muon μ produced in a CC-interaction of a muon-neutrino ν_μ. The photon detection units are illustrated as grey circles.

The number of detected photons is a measure of the intensity of light and can be calculated in dependence of the distance to the emission point d as

$$I(d) = I_0 \cdot \exp\left(-\frac{d}{\lambda_{\text{att}}}\right). \tag{3.7}$$

Therefore the number of photons is reduced and their time residual, which is the time difference between the theoretical expected time assuming no scattering and the measured time, is higher for larger distances. These two points have to be kept in mind for the reconstruction of the lepton direction (see chapter 4).

3.1.4 Types of neutrinos

Three different neutrino flavours (ν_e, ν_μ, ν_τ) exist. All of them can interact via the CC-channel and produce their corresponding lepton which can in principle be detected by the ANTARES detector using the emission of Cherenkov-radiation. For the following reasons, the main neutrino flavour this thesis concentrates on is the muon-neutrino. Electron-neutrinos produce electrons which have a short absorption length and produce a short cascade in water, which means the detection volume is small (for an energy of 1 TeV the path length is ca. 5 m see Fig. 3.2). They can be used for electromagnetic-shower studies. Tau-neutrinos which produce taus have a short lifetime and transform to muons and muon-neutrinos. These cannot be distinguished from muons produced in the CC-interaction of muon-neutrinos and represent background for this reaction. For large-scale neutrino detectors (as for example IceCube [13]) it might be possible to discriminate between tau-neutrinos and muon-neutrinos as in the tau-neutrino case, they might measure two interactions in their detector caused by the tau-neutrino interaction and the interaction of the produced muon-neutrino within their detection volume. For a neutrino detector with a size of 0.01 km^3 as ANTARES this kind of study is nearly impossible.

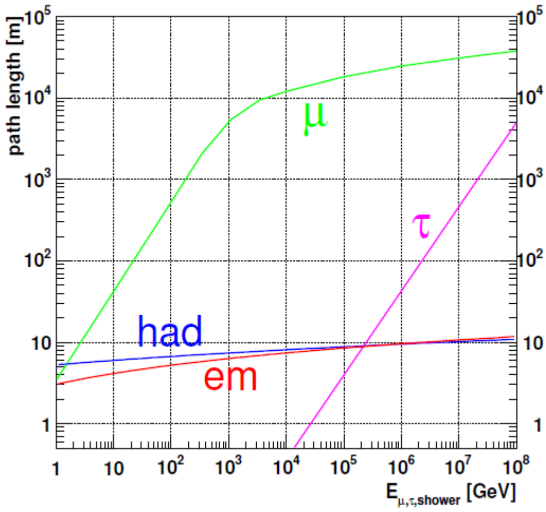

Figure 3.2: Path length in water for muons (green), taus (pink) and electromagnetic (red) and hadronic (blue) showers. Figure taken from [26].

The advantage of muon-neutrinos is that the produced muon can travel kilometers straight through water (see Fig. 3.2) which is good for two reasons. The first is that most muon trajectories have long paths inside the detector, which makes an accurate direction reconstruction possible. And secondly the point of interaction can be far away outside the detector and the muon could still reach it. The detection volume is therefore much larger then the geometric volume of the detector. For the search of point-like neutrino sources, where the direction of the neutrino has to be known with high precision, muon-neutrinos interacting in the CC-channel are the 'golden channel'.

3.2 The ANTARES detector

3.2.1 Detector layout

The ANTARES neutrino telescope is located in the Mediterranean Sea at a water depth of 2475 m ca. 20 km from the coast of south France near Toulon (see Fig. 3.3). It consists of a three-dimensional matrix of 885 photon detection units, the so-called optical modules (OMs), which consist of a pressure resistant glass sphere with a photomultiplier tube (PMT) inside. Always three of these OMs are grouped into a storey with a space angle of 120° between them, with PMTs looking downwards with an angle of 45° to be more sensitive to upgoing neutrino tracks and in order to suppress the atmospheric muon background from above (see section 3.2.4). Fig. 3.4 shows a schematically view of the detector with a picture of one storey. The three-dimensional matrix is fixed by 12 vertical lines, 11 of them containing 25 storeys, one containing 20 storeys and 3 acoustic detection units[1]. The lines are horizontally separated by 60 to 70 m at the seabed and are hold straight by an underwater buoy on top of each line. One line

[1]As part of the ANTARES detector an acoustic neutrino detection test system called AMADEUS is installed, see [27] for details.

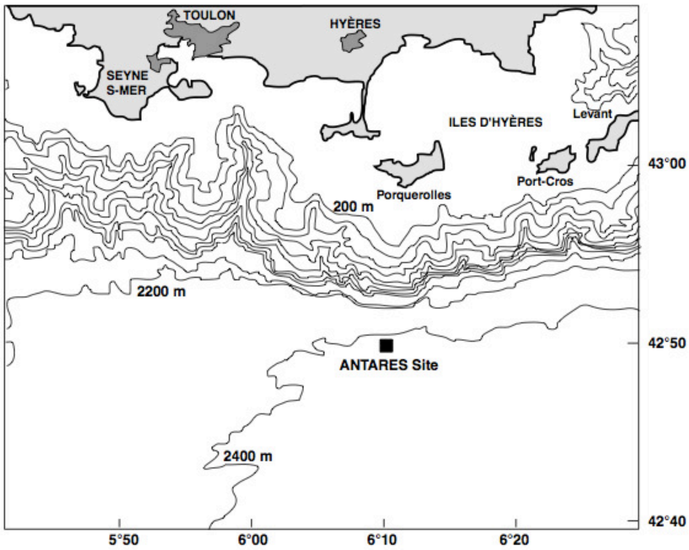

Figure 3.3: Location of the ANTARES detector near the coast of south France in a water depth of 2475 m.

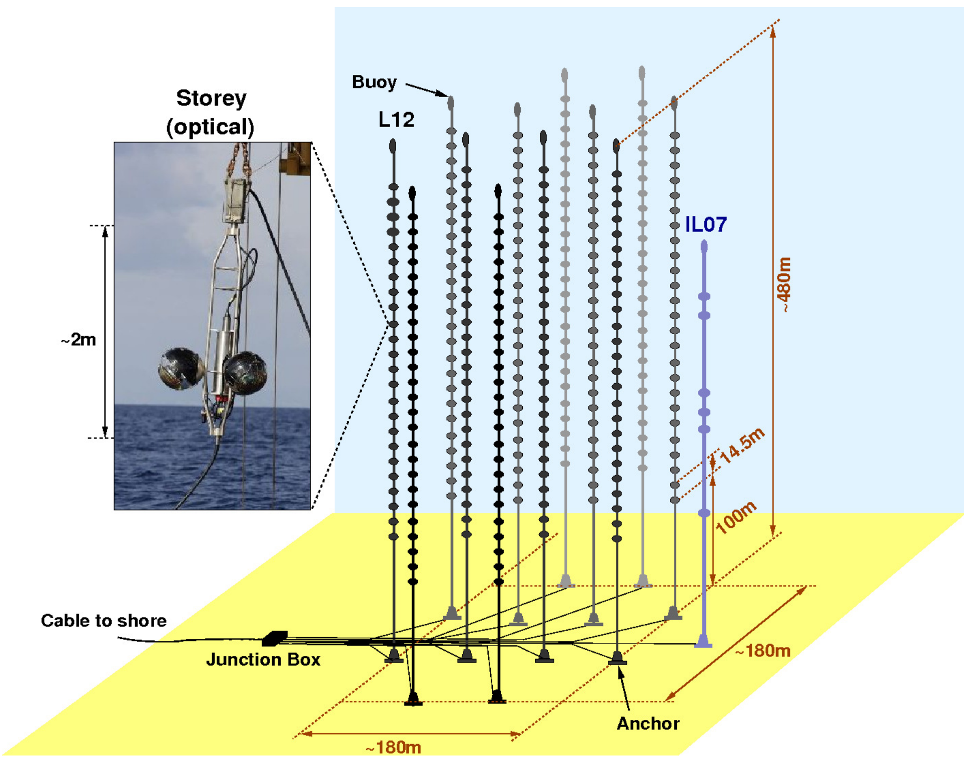

Figure 3.4: A schematical drawing of the ANTARES detector with a picture of one storey.

has a length of ca. 480 m on which 25 storeys are placed at a distance of 14.5 m along the line, the first 100 m above the seabed are not instrumented. In total the detector has an instrumented volume of 0.01 km^3. A detailed description can be found in [28].

3.2.2 Data acquisition and triggering

The measured signals at the PMTs are digitized already at the sea and sent to shore following the all-data-to-shore principle for further processing. The details of these are described in the following.

The electronics of the storey are installed in the LCM (Local Control Module) in the middle between the three OMs. The lines get the power from the 'Junction Box' over an electro-optical cable which has a length of ca. 40 km from the coast station. This cable has also the function of data transmission from the detector to the coast station, where the data are processed and filtered, and sending control data to the detector.

The PMT readout has a fixed threshold which is set to ca. 0.3 pe (photo electrons). If light hits the PMT and its pulse height exceeds the threshold, the pulse is integrated within the integration time of 33 ns[2] [29]. Each PMT has two ARSs (Analogue Ring Sampler) for the readout, which is needed to decrease the acquisition dead time. After the integration time of the first ARS its dead times starts and the second ARS takes over with a short time delay. The ARS transforms the analogue signal to a digital signal by integrating the charge within the integration time, which is called hit. Each hit is stored with a detected arrival time, charge and OM identifier. The charge is correlated with the number of detected photoelectrons whereas the time is synchronized over the whole detector with a precision of 1 ns. All these continuously collected data are send to shore, where a computer farm with filter algorithms (triggers) processes the data current in real time. If the trigger condition of one of the triggers is fulfilled, all data detected within the time window $[t_f - 2.2\,\text{ns}, t_l + 2.2\,\text{ns}]$ are stored on tape as one event, where t_f is the time of the first triggered hit and t_l is the time of the last triggered hit. To run these triggering algorithms in real time a simplified detector configuration of totally straight lines and a non-final calibration, so-called online calibration, is assumed. So the selected data have to be reprocessed with the correct detector geometry and calibration values offline for further analyses as those values can only be determined later on.

Different trigger algorithms are active onshore, they reduce the amount of data by a factor of about 10^4 [28]. The triggers can be divided into different groups: general muon triggers, directional muon triggers for special research purposes, external alert and minimum bias triggers [28]. The general muon triggers are based on a causality criterion (see section 4.1.1) of highly or locally clustered hits or on the coincidence of these hits in next or next-to-next storeys. Some triggeres that are considered for multi-messenger-approach take the position of the source into account. The minimum bias trigger is used to monitor the current detector status and the data quality conditions.

In this analysis only data recorded with general muon triggers are used. As those are independent of the muon direction, the causality of all possible hit combinations is checked. To reduce the computing time for this procedure a preselection of hits is necessary. The hits with either a high charge (typical greater then 3 pe) or hits that are detected on the same storey within a time difference of 20 ns are selected. These hits are called L1 hits (level 1 hits) which is the first trigger level and reduces random background hits substantially. In the case of several coincident hits only the first hit is taken. The general trigger algorithms run with these L1 hits.

[2] The integration time is set to 25 ns after crossing the threshold plus 8 ns before.

If the trigger criterion is fulfilled the corresponding hits are the so-called L2 hits (level 2 hits) and an event containing all triggered hits as well as a snapshot of all hits within the time window mentioned above are recorded.

3.2.3 Influence of environmental conditions

As the Mediterranean Sea is a living environment whose environmental conditions can change in time scales in the order of hours up to seasonal changings, the detector and its performance is influenced by these conditions.

Detector geometry

To determine the muon trajectory with high precision the timing resolution must be in the order of a few nanoseconds and the position of each OM has to be known with a precision of a few tens of centimeters. As the detector lines are flexible (only hold straight by a buoy and fixed at the seabed) they can bend correlated with the velocity of the sea current, so that they differ from the geometry of a straight line. In addition the storeys can rotate around the cable of the line. To determine the actual position and orientation of each OM a hybrid positioning system is used. The acoustic positioning system consists of emitters at the seabed and at the anchor of each line and hydrophones on every fifth storey of each line that detect the acoustic signals. Through trilateration the position of each storey can be reconstructed with a precision better then 10 cm. Fig. 3.5 shows the reconstructed position of the storeys of one line for different values of the velocity of the sea current, a typical value is 5 cm/s. The compass-tiltmeter system installed on every storey determines the orientation and inclination of the storey. A detailed description can be found in [30].

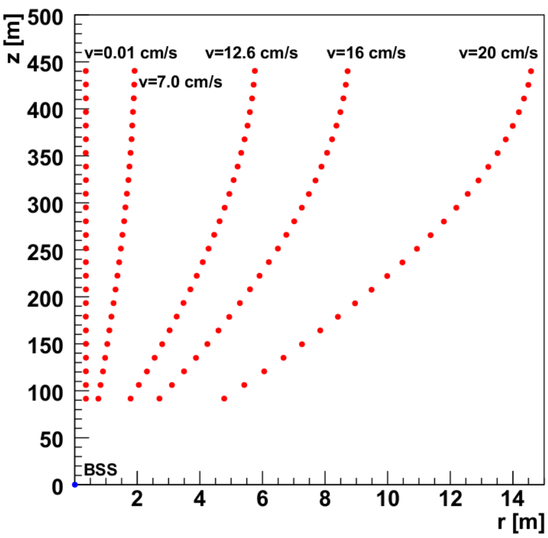

Figure 3.5: Reconstructed position of the storeys of one line with the acoustic positioning system for different sea currents. Figure taken from [30].

Optical background conditions

There are two different types of optical background. One is the decay of ^{40}K which is solved in the seawater and the other is bioluminescence, light emitted by living organisms such as bacteria, pyrosoma and plankton or some fish species [31]. The part of the optical background rate caused by ^{40}K is almost constant over time as the concentration of ^{40}K is constant (only slight changes due to exchange of water). But the contamination of the background rate caused by bioluminescence depends on the season and the sea water current. The first is due to the fact that for example in spring new feed flows from the Alps into the sea and animates the deep-sea fauna to emit light. On smaller time scales, the optical background rate changes due to the sea current as the animals are stimulated to emit light by hitting a detector structure, where the probability of hitting an OM rises with the turbulence around the structure. Typical background baseline rates are in the range from 50 to 100 kHz, whereas some short and local burst can have rates up to 1 MHz (see Fig. 3.6). As these rates vary with time and sea current the minimum bias data are taken to determine the status of the background conditions. The optical background are hits caused by these effects. To take these varying conditions into account a dedicated run-wise MC simulation is done for each run separately (see section 6.3).

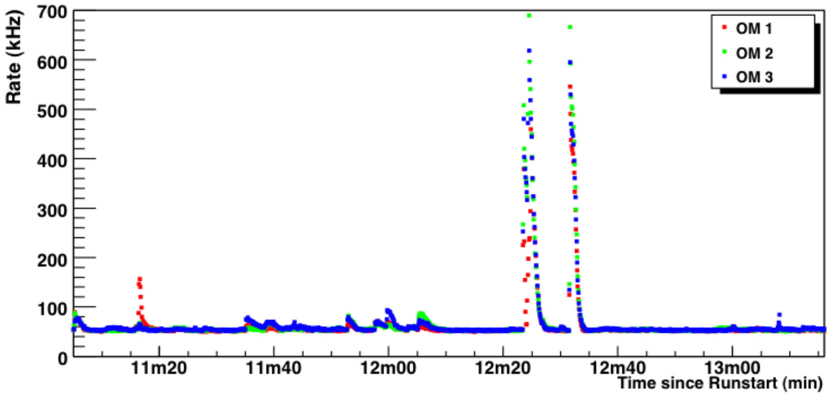

Figure 3.6: Rate of detected photons at the different OMs of one storey. Figure taken from [32].

3.2.4 Signal and background events

The ANTARES detector can measure signatures caused by muons traversing or passing the detector, which is called a signal. These muons are atmospheric muons or muons generated by cosmic or atmospheric neutrinos (neutrino signal). The different event types are shown in Fig. 3.7 and are described in the following. When talking about signal neutrinos, cosmic neutrinos are meant.

Cosmic and atmospheric neutrinos

The generation of both cosmic and atmospheric neutrinos follows the same interaction processes starting with the decay of a charged pion interacting with atoms in the interstellar medium or respectively in the atmosphere and producing muon-neutrinos and muons, which themselves can decay in a second process into electrons and electron-neutrinos as already discussed in chapter 2 see eqn. (2.2) and eqn. (2.3).

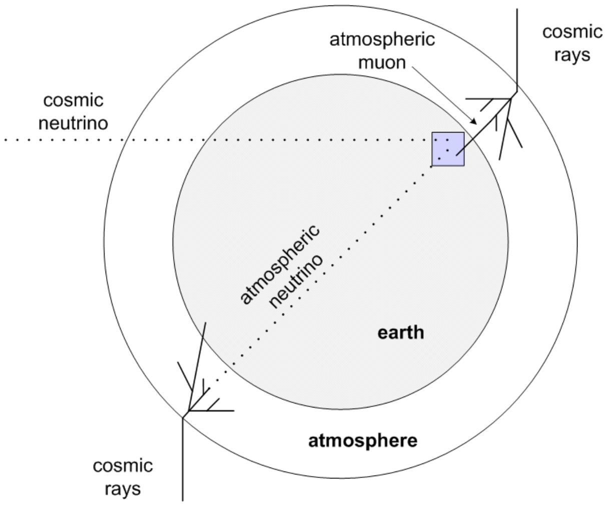

Figure 3.7: Schematic view of possible event sources detected with the ANTARES detector. Figure taken from [32]

If these neutrinos are created in the interaction of cosmic rays with the atmosphere they are called atmospheric neutrinos which are expected to follow an $E^{-3.7}$ spectrum. Cosmic neutrinos created by cosmic sources explained in chapter 2 are expected to generally follow an E^{-2} spectrum from Fermi-acceleration if no prediction for the neutrino flux shape per source candidate can be derived. Both cosmic and atmospheric neutrinos can reach the detector from every direction as their cross-section is very low, so that they can also traverse the Earth and reach the detector from below (see Fig. 3.7). Atmospheric neutrinos are isotropically distributed over the full sky. Even if they correspond to a neutrino signal these neutrino events are background events in the view of a search for cosmic neutrinos from point-like sources.

After the detection of a neutrino event one cannot discriminate between cosmic and atmospheric neutrinos. Therefore statistical methods are necessary to distinguish between them. In this thesis a maximum-likelihood-based analysis method using hypotheses testing is used. It takes the hypothesis of only background events (atmospheric neutrinos) as null hypothesis and evaluates if the measured signal is in agreement with this hypothesis or not (see chapter 7).

Atmospheric muons

If muons produced in charged pion decays (eqn. (2.2)) in the atmosphere of the Earth do not decay further, they can reach the Earth and also the detector. As their travel distance in earth, caused by their energy loss, is small, this can only be from above. So they are absorbed in the Earth and one uses the Earth as shield from atmospheric muons by using only upwards going, short upgoing, events. As the rate of atmospheric muons from above is about a factor 10^6 higher then the atmospheric neutrinos (see Fig. 3.8), the reconstructed direction of the muons is the main parameter used to discriminate between neutrinos and atmospheric muons, being aware of loosing neutrino events coming from above. Further methods could be using only starting tracks or contained events within the detector. But for neutrino energies above 1 TeV these new methods are only possible for large scale detectors such as IceCube or KM3NeT.

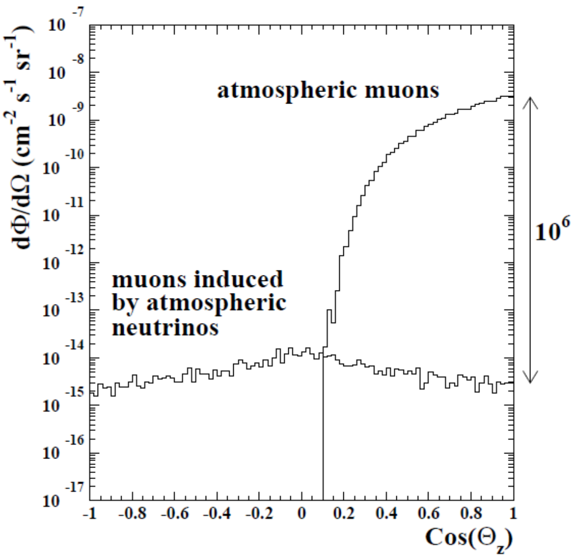

Figure 3.8: Zenith distribution of the muon flux for energies above 1 TeV for atmospheric muons and atmospheric neutrino induced muons in a depth of 2300 m in water. Figure taken from [24].

Chapter 4

Development of a myon track reconstruction algorithm

There are two standard track reconstruction strategies for ANTARES. One of these is a fast track reconstruction algorithm that is also used for online reconstruction of some events, called BBFit [33]. As this reconstruction has to be done in real time it is less accurate using for example the assumption of straight lines and the OMs are located at the center of the storey by ignoring the actual position of the OMs determined by the alignment process (see section 3.2.3). For offline reconstruction with this fit the position of the storeys is taken into account. In principle this strategy is based on a χ^2-fit with a modified χ^2-function. Its resolution for events reconstructed with hits on more than two lines is about 0.94° for an E^{-2} neutrino flux after applying quality cuts [33]. The other reconstruction strategy, called AAFit [34], uses the maximization of a likelihood starting with a robust prefit and a sequence of further prefit steps whose result is used as reference direction for the maximization of a likelihood. It has a resolution of about 0.4° for an E^{-2} neutrino flux after applying quality cuts [35].

A new concept of scanning the whole phase space in Θ and Φ in discrete steps and find the position of such a track fitting best to the hits of the event for one particular direction is established in this thesis. Such a track reconstruction algorithm called FilteringFit was developed and optimized by Claudio Kopper for a proposed geometry of the future KM3NeT detector, which showed promising results [36]. During this thesis this kind of fit was developed for the ANTARES detector to use as a prefit input for an high-resolution maximum likelihood fit. Getting more or additional information for one event of an additional fit to the standard ones, can increase the number of neutrino events for an point source analysis for example.

In this chapter the concept of the FilteringFit track reconstruction algorithm is explained, its adaptation and enhancement to be used as prefit for the ANTARES detector is described and its performance using an additionally maximum likelihood fit as final fit, as compared to the standard track reconstruction strategies of ANTARES, is shown.

4.1 The FilteringFit track reconstruction algorithm

The FilteringFit track reconstruction is based on scanning the whole phase space by generating a discrete number of track hypotheses (Θ, Φ) which are isotropically distributed over the sky. Fig. 4.1 shows an overview of its fitting procedure. For each of these directions an hit selection is performed using the largest number of causally connected hits. For this hit selection the

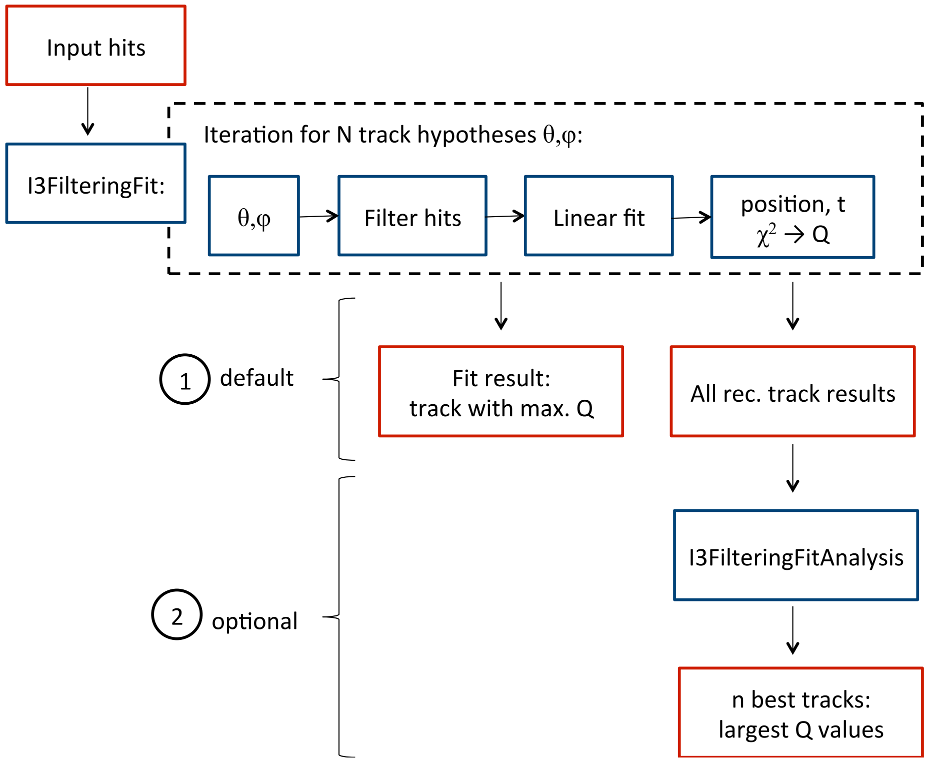

Figure 4.1: Overview of the FilteringFit track reconstruction algorithm. The default path is marked with 1, the optional path is marked with 2 for further reference.

position of the given direction for a point of time is fitted by a linear fit (according to [37]). A quality parameter Q is calculated for each hypothesis in order to determine the best fitted track assumption. The number of tested directions can be changed, changing the space angle between the different directions accordingly, and is therefore correlated with the resolution of the fit. In the following the separate parts of the fitting procedure per track assumption is explained in more detail. To simplify the problem the coordinate system is rotated so that the z-axis is pointing along the muon direction and is transformed back after the fitting process.

4.1.1 Hit selection: filtering of hits

The hit selection is based on a causality criterion where hits that are correlated in time and position are taken, the others are filtered out[1]. This procedure follows the clustering procedure of the so-called 3N trigger described in [38].

To calculate the expected arrival time t_i of an hit i at OM_i at position $(x_i,\ y_i,\ z_i)$ to a assumed muon direction, it is convenient to rotate the coordinate system such that the muon

[1]Caused by this filtering of hits, the fit got its name.

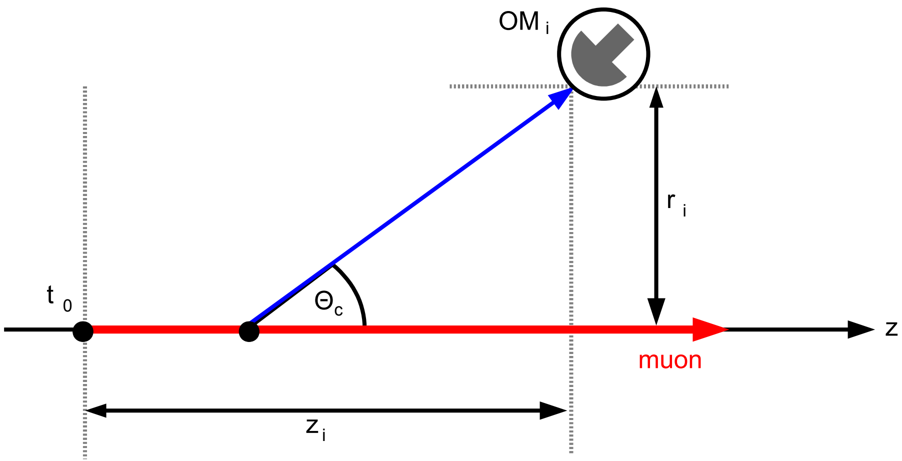

Figure 4.2: Definition of the geometric parameters for one emitted and detected photon at OM_i in the rotated coordinate system, where the muon direction is identical with the z-axis.

direction points along the z-axis. Then t_i is given by

$$t_i = \underbrace{t_0}_{\text{reference time}} + \underbrace{\frac{1}{c}\left(z_i - \frac{r_i}{\tan\Theta_c}\right)}_{\substack{\text{time the muon needs to}\\ \text{travel to the photon emission point}}} + \underbrace{\frac{1}{v_g}\frac{r_i}{\sin\Theta_c}}_{\substack{\text{photon travel time from}\\ \text{the emission point to the OM}}} , \tag{4.1}$$

where z_i is the position along the muon track, r_i the perpenticular distance of the OM from the muon track (see Fig. 4.2), $v_g = c/n_g$ is the group velocity (c is the speed of light, n_g is the refractive index of water) and Θ_c the Cherenkov-angle in water. This formula simplifies to

$$t_i = t_0 + \frac{1}{c}(z_i + \kappa r_i) \text{ with } \kappa = \frac{c}{v_g \sin\Theta_c} - \frac{1}{tan\Theta_c} = \frac{n_g}{\sin\Theta_c} - \frac{1}{tan\Theta_c}. \tag{4.2}$$

So for two hits on two OMs the minimal perpendicular distances to the muon track r_1 and r_2 are unknown as only the direction but not the position of the muon is given. But the maximal distance between them in the xy-plane $R = \sqrt{(x_2 - x_1)^2 + (y_2 - y_1)^2}$ is known. So it follows for the time difference

$$\underbrace{(t_2 - \frac{z_2}{c}) - (t1 - \frac{z_1}{c})}_{\Delta t} \leq \frac{\kappa}{c} R. \tag{4.3}$$

Including an extra time t_{extra} for time calibration uncertainties and scattering the criterion used in the FilteringFit algorithm is

$$\left(\Delta t_{corr} \cdot \frac{c}{\kappa}\right)^2 \leq R^2, \tag{4.4}$$

with $\Delta t_{corr} = |\Delta t| - t_{\text{extra}}$. Additionally to this criterion one can apply an maximal allowed distance between two hits $R < d_{\max}$.

The first step of the fitting procedure after rotating the coordinate system into the muon track direction is the filtering of the hits due to the criterion from eqn. (4.4). All hit pair combinations are tested to this criterion iteratively starting with one of the hits and finding the hits causally connected to it, which defines a cluster. The cluster of hits with the largest number of hits N_{hits} is taken for the actual fitting of the position of the muon track in the next step.

4.1.2 Linear fit

In the rotated coordinate system, fixing the direction (Θ, Φ) of the track, the original 5-dimensional problem becomes a 3-dimensional problem: finding the position of the muon track along the z-axis (x,y,t). This can be done with a linear fit described in [37]. In principle the task is to solve a linear system of equations $H\vec{p} = \vec{y}$, where $\vec{p} = (x_0, y_0, t_0)$ is the position of the muon track and $\vec{y}$ is a vector containing all hits (x_i, y_i, t_i).

$$H = \begin{pmatrix} 2(x_2 - x_1) & 2(y_2 - y_1) & -2(t_2 - t_1) \\ 2(x_3 - x_2) & 2(y_3 - y_2) & -2(t_3 - t_2) \\ . & . & . \\ . & . & . \\ 2(x_1 - x_n) & 2(y_1 - y_n) & -2(t_1 - t_n) \end{pmatrix} \tag{4.5}$$

$$\vec{y} = \begin{pmatrix} x_2^2 - x_1^2 + y_2^2 - y_1^2 - t_2^2 + t_1^2 \\ x_3^2 - x_2^2 + y_3^2 - y_2^2 - t_3^2 + t_2^2 \\ . \\ . \\ x_1^2 - x_n^2 + y_1^2 - y_n^2 - t_1^2 + t_n^2 \end{pmatrix} \tag{4.6}$$

This can be derived from eqn. (4.1), that can be rewritten as

$$t_i = t_0 + \frac{z_i - z_0}{c} + \tan(\Theta_c)\frac{r_i}{c}, \tag{4.7}$$

with the perpendicular distance to the track $r_i = \sqrt{(x_i - x_0)^2 + (x_i - x_0)^2}$. By taking the following substitutions $t'_0 = t_0 c/\tan(\Theta_c)$ and $t'_i = t_i c/\tan(\Theta_c) - (z_i - z_0)/\tan(\Theta_c)$ one can convert eqn. (4.7) to

$$(t'_i - t'_0)^2 = (x_i - x_0)^2 + (x_i - x_0)^2. \tag{4.8}$$

Calculating the difference of eqn. (4.8) for two different hits one gets

$$t'^2_j - t'^2_i - 2(t'_j - t'_i)'_0 = x_j^2 - x_i^2 - 2(x_j - x_i)x_0 + y_j^2 - y_i^2 - 2(y_j - y_i)y_0, \tag{4.9}$$

which is one of the linear equations that has to be solved. This can be formulated as $H\vec{p} = \vec{y}$ with the matrix H defined in eqn. (4.5) and $\vec{p}$ defined in eqn. (4.6) taking the respective substitutions for t' instead of the time t.

As the matrix H combines the time and position differences of two consecutive hits per row the ordering of the hits is important. They are therefore ordered before inserting in eqn. (4.5) and eqn. (4.6) by the polar angle with respect to their center of gravity and interleaved to have the maximal difference between them [39]. The $\vec{p}$ of equation $H\vec{p} = \vec{y}$ is the fitted muon position for this particular direction (Θ, Φ) for which the quality parameter χ^2 is calculated as

$$\chi^2 = \frac{\sum_{i=1}^{N_{\text{hits}}} t_{\text{res},i}^2}{\sigma^2} = \frac{\sum_{i=1}^{N_{\text{hits}}} (t_{i,\text{theo}} - t_{i,\text{meas}})^2}{\sigma^2}, \tag{4.10}$$

where $t_{\text{res},i}$ is called the time residual calculated by the difference of the expected arrival time $t_{i,\text{theo}}$ (see eqn. (4.1)) and the measured time of the hit $t_{i,\text{meas}}$, and $\sigma = 2\,\text{ns}$ which is a measure of the time resolution of the PMT.

4.1.3 Quality parameter

A modified quality parameter Q is calculated using the resulting χ^2 as

$$Q = N_{\text{hits}} - w \cdot \frac{\chi^2}{\text{NDoF}}, \tag{4.11}$$

where N_{hits} is the number of hits used for the fit, $\text{NDoF} = N_{\text{hits}} - 3$ is the number degrees of freedom for 3 free parameters and w is a weighting factor which can be set by the user. As the hits used for fitting are causally correlated with respect to the track direction, a track hypothesis with a large number of hits used for fitting should fit the event better, than a track hypothesis with less causally connected hits. Therefore this is included in the quality parameter Q, which assigns a track assumption with many hits a better quality than an assumption with less hits and a good χ^2 value. On the other hand as N_{hits} is an integer number, a low χ^2 helps to decide between direction with a similar number of hits as fine tuning. The parameter w can be used to fine tune the influence of the χ^2.

4.1.4 FilteringFit result

For each track hypothesis the steps of the hit selection, linear fit and the calculation of Q is performed. The fit provides the possibility to use several outputs, shown in Fig. 4.1 with a default path (path 1) and an optional path (path 2). As default output the track hypothesis with the largest Q value is taken as fit result, which is named as 'maxQ' in the following. In addition to the fit result the parameters of all reconstructed track hypotheses are stored in a vector class, which allows for the analysis of all performed fitting steps. This is done with the SeaTray[2] module 'I3FilteringFitAnalysis' as shown in Fig. 4.1, optional path. One option of this module is to select the fitting results of the tracks with the n best Q values. A minimal allowed distance between the tracks, considered for this selection, can be set to ensure that the n best tracks are spacial separated by at least that angle.

4.2 The high-resolution muon track reconstruction: KrakeFit

The aim in developing KrakeFit was to adapt the FilteringFit reconstruction strategy to be used as a prefit for a final fit which uses a maximum likelihood-based method. The resolution of the prefit should be about 1° as studies of an analytical PDF (probability density function) give this number as the maximum angular distance where this PDF can converge. For this purpose the

[2]SeaTray is the ANTARES software framework [40] adapted from the icetray software framework of IceCube [41].

FilteringFit module was extended in this study and compared to BBFit [33] for a small neutrino sample. Furthermore, a maximum-likelihood-based fit was applied to reach a higher resolution. In this section the different steps of the prefit and the final fit are explained, which is in total called 'KrakeFit'.

Definitions for plots

For this study a small sample[3] of upgoing neutrino events that are triggered by at least one of the standard ANTARES triggers (3N and/or 2T3 [42], [43], [44]) were used. An optical background of 60 kHz random noise and a fully working detector were assumed. The neutrinos have energies in the range between 1 TeV and 1 PeV and are weighted according to an E^{-2} energy spectrum. The angle between the true and the reconstructed muon direction is called $\Delta\alpha$ in the following. When talking about well-reconstructed events, those with an angular error $\Delta\alpha < 6°$ are meant. With efficiency the efficiency of well-reconstructed events is meant, if not stated differently, it is defined as follows

$$\text{efficiency} = \frac{\text{reconstructed events with } \Delta\alpha < 6°}{\text{all triggered events}}. \tag{4.12}$$

4.2.1 Performance of FilteringFit for ANTARES

As explained in the previous section 4.1, there are several parameters that can be tuned in FilteringFit and they have to be adapted for the ANTARES detector. For this purpose each of these parameters was optimized with respect to the median of the angular error, by holding the other parameters fixed. By this procedure the following parameters are found to work best for ANTARES.

As input hits for starting the hit selection not all detected hits are used as the cluster algorithm is quite time consuming, so the time of fitting scales factorial with number of input hits [39]. Further without a preselection of hits, the number of background hits is high (at a background rate of 60 kHz the mean number of background hits is about 260) which could fulfill the causality criterion just by chance. That minimizes the chance of finding the best cluster of hits fulfilling this criterion per direction. It turns out that the strict L1 hit criteria is a good choice as input for the hit selection for the studied high-energy regime as the number of signal hits is still high[4] (for low-energy events it might be different [32]). The minimum number of hits in a cluster for each direction is set to 6 hits to start the linear fit process, as in the non-linearized problem 5 parameters have to be fitted and at least 6 hits are needed to solve this problem. This number is not changed even though only 3 parameters have to be fitted once the direction (Θ, Φ) is fixed. The parameters $t_{\text{extra}} = 5$ ns and $d_{\text{max}} = 300$ m have been chosen, the latter is practically no limit on the transverse distance as the OMs are installed at about 350 m along one line (see Fig. 3.4 in section 3.2). The number of directions used in the fit (NumIterations) work best at 60000, as the distance between two track assumptions is smaller than 1°. For the calculation of the Q value, the weight w is set to 0.5. For the optional path the parameters were set that 10 tracks with the best Q values are selected that have a minimal distance of 1°

[3] 10^{10} neutrino events were generated for an energy range between 10 GeV and 10^7 GeV.

[4] The L1 hit selection collects roughly 50% of the signal hits with a purity better than 90% for an background rate of 60 kHz; the mean number of signal hits included is about 20 (70) for neutrinos with energies between 1 TeV to 10 TeV (100 TeV to 10^3 TeV).

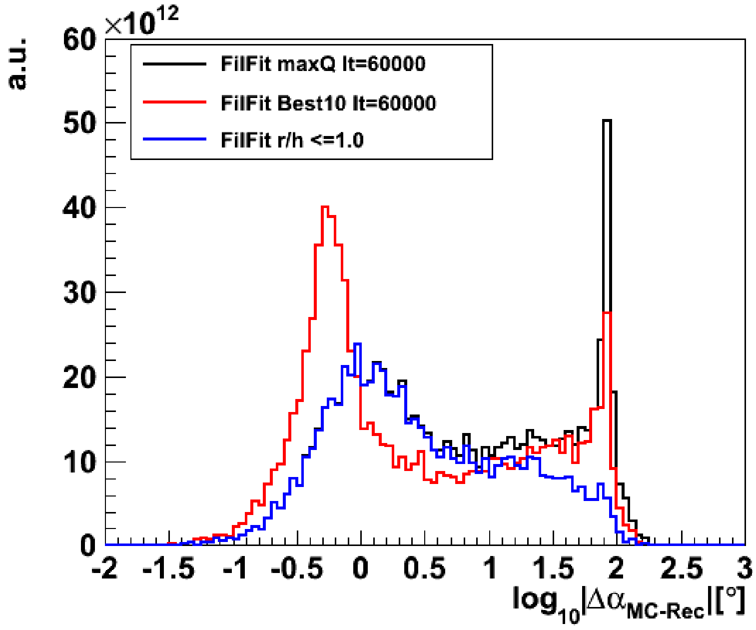

Figure 4.3: Distribution of $\log_{10}\Delta\alpha$ for the FilteringFit result maxQ (black), the best of the 10 best tracks (red) and for the FilteringFit result maxQ without tracks where $r/h > 1.0$ (blue), events are weighted according to an E^{-2} spectrum.

between them. If in the plots the label 'Best$n$' is used it means that the track with the minimal $\Delta\alpha$ out of the n best FilteringFit tracks is used for plotting[5].

The resulting angular error $\Delta\alpha$ of the FilteringFit is shown in Fig. 4.3 (black curve) exhibiting a strong peak at 84°. The assumption is that this is attributed to mirror solutions, which can appear if the pattern of hits used to fit the track forms a symmetry plane. These symmetries can be identified if the rank of the tensor of inertia calculated for the used hits is smaller than 3. It turned out that only 50% of the entries of the peak can be identified by this criterion. So a new or additional criterion is needed to identify badly reconstructed tracks, which will be discussed in section 4.2.2.

For the red curve in Fig. 4.3 and Fig. 4.4 the track with the minimal $\Delta\alpha$ within the 10 best tracks was used. The main peak of the angular error distribution in Fig. 4.3 (red curve) is shifted to lower angular errors compared to the standard FilteringFit result (black curve). This means that within the 10 best tracks there is most of the time at least one track that is nearer to the true muon direction than the standard FilteringFit result 'maxQ'. Therefore one could gain in precision by using the 10 best tracks instead of the final fit result of the FilteringFit for the next step. This requires a criterion to identify the track with the minimal angular error within these 10 tracks, which is discussed in section 4.2.2.

[5]It is worth to mention that here MC information is used to determine the track with the minimal $\Delta\alpha$ out of the n best tracks only for the plotting purpose. It is not used in the fitting procedure itself.

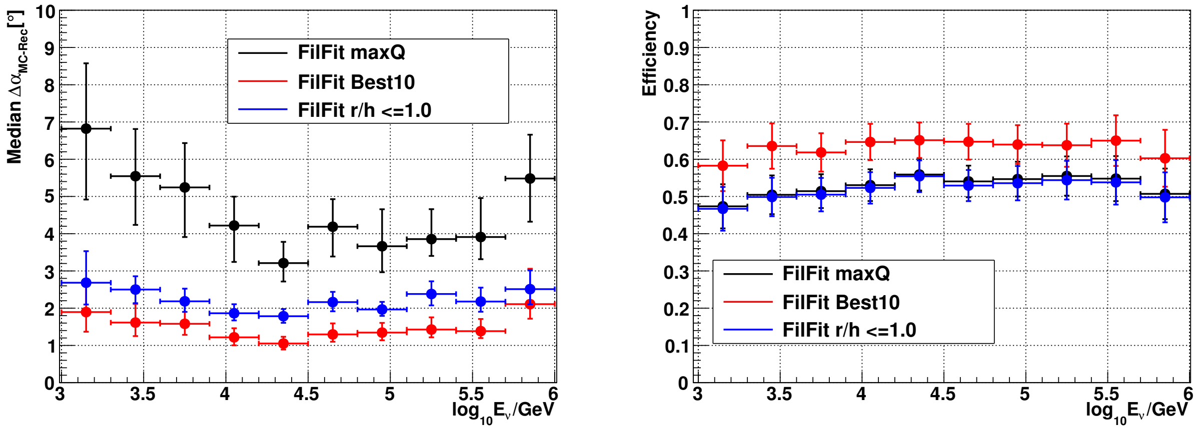

Figure 4.4: Left: Median of the angular error $\Delta\alpha$ for different neutrino energies E_ν/GeV; right: efficiency of reconstructed events with $\Delta\alpha < 6°$ for different neutrino energies E_ν/GeV. Both for FilteringFit result maxQ (black), the best of the 10 best tracks (red) and for the FilteringFit result maxQ without tracks where $r/h > 1.0$ (blue).

4.2.2 Extension of the FilteringFit reconstruction chain

Criterion to identify badly reconstructed tracks: cylinder criterion r/h

The following criterion showed to be effective indentifying badly reconstructed events: For every reconstructed track direction L1 hits are selected with time residuals between $-5\text{ns} \leq t_{\text{res}} \leq 20\text{ns}$. The time residual t_{res} is the difference of the measured time of the hit and its theoretical time t_{theo} which can be calculated with eqn. (4.1). One can define a cylinder around each track with minimal radius r and minimal height h containing all the selected hits. The assumption for neutrinos with energies above 1 TeV is that these hits lie along the track within a small distance. The reason is that high-energy neutrinos produce muons with long travel distances through the detector; the larger the distance of the detected photons to the muon track, the higher is the probability of scattering. Therefore hits with small time residuals lie along the track with relatively small distance compared to the long track lengths. Reconstructed muon tracks that have a larger cylinder radius than height are expected to be misreconstructed (Fig. 4.5 shows two different track assumptions for the same hit pattern and the corresponding cylinder containing these hits). Therefore tracks with cylinder criterion $r/h > 1.0$ are disregarded. In Fig. 4.3 the distribution of the angular error is shown in black without r/h cut and in blue with r/h cut. One can see that most of the badly reconstructed tracks are rejected without losing well-reconstructed tracks. For tracks reconstructed with angular errors smaller than 5° 98.8% of events remain, but tracks reconstructed with angular errors larger than 5° (60°) only 56.5% (20.5%) survive this cut. This can also be seen in Fig. 4.4 in the right plot, where the efficiency of well-reconstructed tracks is shown. There is almost no difference between the black and the blue curve. Further in the left plot of Fig. 4.4 the median of the blue line is (as expected) better and gets closer to the median of the red curve, which defines the optimum obtainable by the strategy.

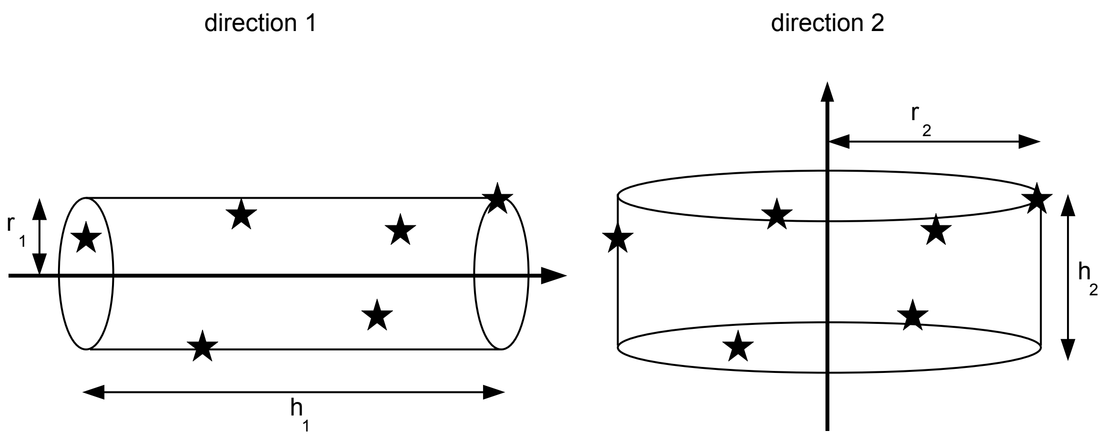

Figure 4.5: Schematic drawing of cylinders with radius r_i and height h_i calculated around two different track hypotheses with the same hit pattern.

Criterion to identify a well-reconstructed track within the n best tracks: surface density criterion (sD)

The cylinder criterion can be used as a preselection of tracks out of the n best tracks. The next step is to have a criterion to find the best track within the selected ones. This is performed using the surface density (sD) which is defined as

$$sD = \sum_{i=1}^{3} \frac{N^2_{\mathrm{hits,r_i}}}{\sum\limits_{\mathrm{OMs}} AngAcc_{r_i}}, \tag{4.13}$$

where $N_{\mathrm{hits,r_i}}$ is the number of hits and $\sum\limits_{\mathrm{OMs}} AngAcc_{r_i}$ is the sum of the angular acceptance of the OMs within in a cylinder with radius r_i around the track. The chosen values for the three radii determined by optimization are $r_1 = 2.0 \cdot 55.0\,\mathrm{m} \cdot \sin\theta_c$, $r_2 = 1.5 \cdot r1$, and $r_3 = 2.0 \cdot r1$, motivated by the absorption of light in seawater (see section 3.1.3). Eqn. (4.13) is adapted from [45] where it was established for low-energy events. The underlying idea is the same as for the cylinder criterion. The number of hits around the track decreases exponentially with the distance to the track. The fraction of detected hits over the sum of OMs that could have detected light should be higher for inner cylinders than for outer cylinders. Eqn. (4.13) takes this into account. Instead of using the number of OMs within the cylinder the angular acceptance of the OMs, which is the detection probability of light depending on the angle of impact at the PMT (ranges from 0 to 1), assuming direct photons from the track, is used as OMs hit for example from the back should not be taken into account. If one track assumption doesn't fit the true muon direction well, this fraction should be small and therefore its sD value will be small compared to a track assumption which is closer to the truth. The sD value is calculated for each track and the one with the largest sD value is selected.

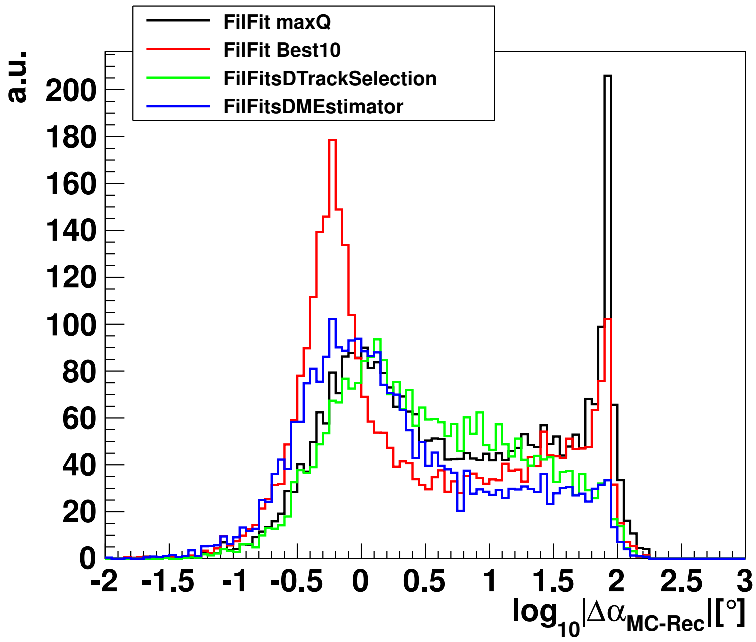

Figure 4.6: Distributions of $\log_{10}\Delta\alpha$ for the FilteringFit result maxQ (black), the best of the 10 best tracks (red), the FilteringFitsDTrackSelection result (green) and FilteringFitsDMEstimator result (blue).

Combination of r/h and sD: FilteringFitsDTrackSelection

After some tests it turned out that the combination of the r/h and the sD criteria gives the best results. This combination is implemented as a SeaTray module called 'FilteringFitsDTrackSelection' in the filteringfit project. The n best tracks are first filtered so that only tracks that fulfill the r/h criterion are passed to the calculation of the sD value, where the track with the maximum sD is taken as result. This means that events where none of the n best tracks fulfills the cylinder criterion are lost. The combination with the sD criterion enhances the performance compared to using only the maxQ tracks that pass the r/h cut, because the total efficiency is increased[6]. The distribution of $\Delta\alpha$ for this step is shown in Fig. 4.6 (green curve).

Improving the resolution: MEstimator fit

In the AAFit [34] and the BBFit [33] reconstruction algorithms, applying an MEstimator fit results in an improvement in angular resolution. The MEstimator downweights outliers in the fit and with this improves the angular resolution by maximizing $\sum_{\mathrm{i}=1}^{N_{\mathrm{hits}}} g(t_{\mathrm{res},i})$ with

$$g(t_{\mathrm{res},i}) = -2\sqrt{1+\frac{t_{\mathrm{res},i}^2}{2}}+2, \tag{4.14}$$

[6]As an example if the maxQ track doesn't fulfill the r/h criterion, the event would be rejected. But if the n best tracks are used, there is still the chance, that one of the other $n-1$ best tracks of this event fulfills this criterion and so it won't be filtered out.

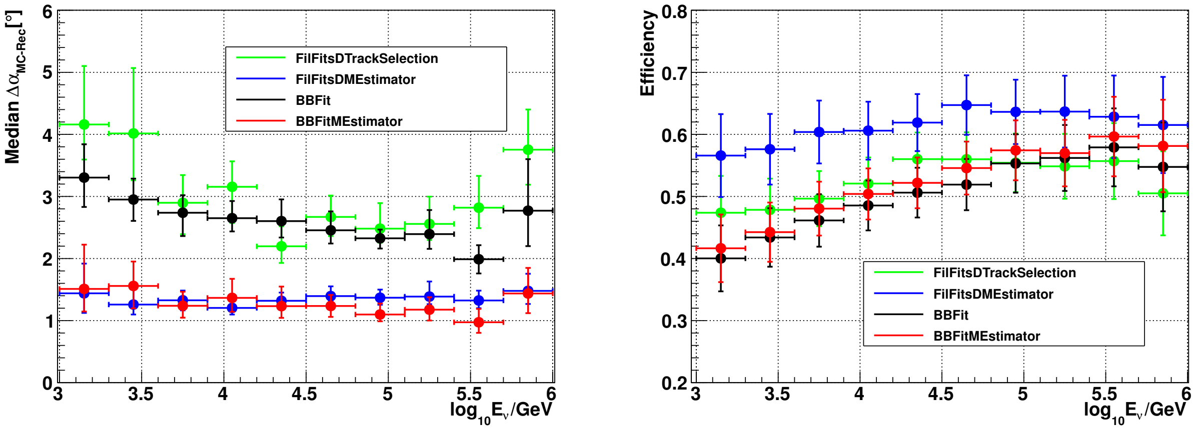

Figure 4.7: Left: Median of the angular error $\Delta\alpha$ for different neutrino energies E_ν/GeV; right: efficiency of reconstructed events with $\Delta\alpha < 6°$ for different neutrino energies E_ν/GeV. Both for FilteringFitsDTrackSelection (green), FilteringFitsDMEstimator (blue), BBFit (black) and BBFitMEstimator (red).

where $t_{\text{res},i}$ (in ns) is the time residual of the hit. This function is linear in t_{res} for large value of t_{res}, but quadratic for small values of t_{res}. Therefore hits with larger time residuals have less influence in the result of the fit than hits with small time residuals. As the AartStrategy [34] is implemented as a chain of single modules in SeaTray and it is possible to use its individual parts also in other reconstruction chains, its hit selection and MEstimator are used here.

The output of the n best tracks after applying the r/h and sD track selection (FilteringFitsDTrackSelection) was used as a reference direction for the hit selection and the MEstimator fit. As can be seen in Fig. 4.6, the use of the MEstimator (blue curve) moves the main peak to lower angular errors and thus the resolution improves by using this fit. In Fig. 4.7, the median angular error is shown for all reconstructed events on the left and the efficiency of well-reconstructed events (events reconstructed with angular errors less then 6°) are shown on the right. In comparison to Fig. 4.3 and Fig. 4.4, one can see an improvement in the resolution as well as the efficiency for well-reconstructed events. In the plots the BBFit and BBFitMEstimator results are also shown. The FilteringFitsDMEstimator gives comparable results for the median of the angular error and improves the efficiency compared to BBFitMEstimator, where no quality cuts are applied[7]. One can see an improvement of the FilteringFit reconstruction chain for high-energy neutrino events with this extension of the reconstruction chain, whose result will be called 'FilteringFitsDMEstimator' and has a resolution for neutrino energies above 1 TeV between 1.2° and 1.5°. It is the prefit of an high-resolution track reconstruction chain, which is shown in the following section.

[7]BBFit single-line events are disregarded here as only the zenith but not the azimuth could be determined for such events with that strategy. So the space angle between reconstructed track and the muon direction cannot be calculated.

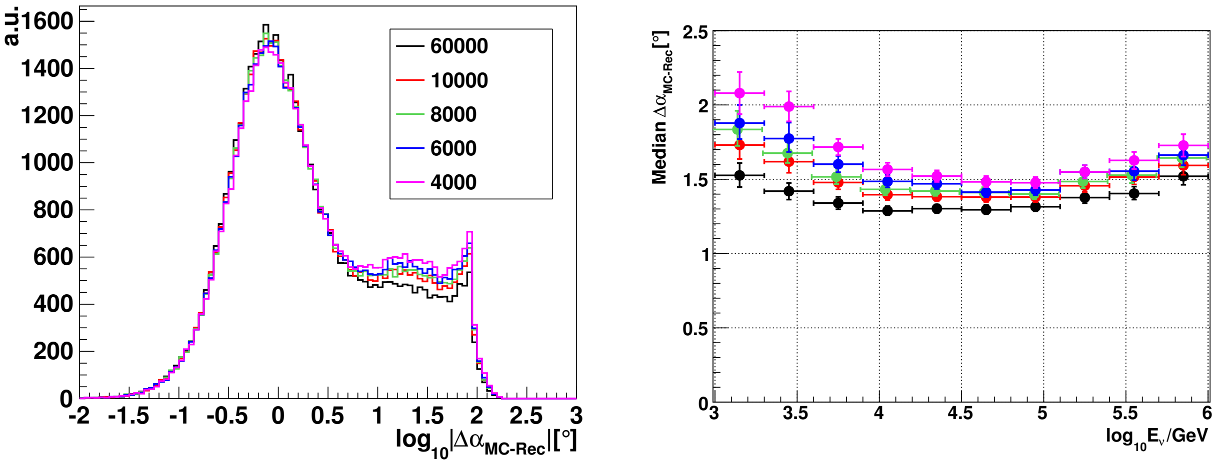

Figure 4.8: Left: Distribution of $\log_{10} \Delta\alpha$; right: median of the angular error $\Delta\alpha$ for different neutrino energies E_ν/GeV. Both for the FilteringFitsDMEstimator result after applying different numbers of track directions 60000 (black), 10000 (red) 8000 (green), 6000 (blue) and 4000 (pink) in the FilteringFit step.

4.2.3 Overview of the total track reconstruction algorithm

As shown in the previous section, the prefit starting with the FilteringFit module and ending with the MEstimator fit shows good results. The fitting procedure is time consuming, where the computing time is dominated by the FilteringFit step. The CPU time per event depends on the number of directions used for the fit as for each of them the hit selection and linear fit has to be performed. To decrease the computing time, this number was reduced to find an optimal value while still having a good resolution after the MEstimator step. Fig. 4.8 (left) shows the distribution of $\log_{10}\Delta\alpha$ for the 'FilteringFitsDMEstimator' step for different numbers of iterations set in the FilteringFit part. On the right plot the median of the space angle error is plotted versus the neutrino energy. Combining these two plots one can deduce that the lower the number of iterations, the worse the resolution gets. A good compromise between resolution and computing time is using 10000 iterations instead of 60000 per event. The mean computing time per event for $E_\mu = 1\,\text{TeV}$ is then approximately 0.3 s and for $E_\mu = 10\,\text{TeV}$ is approximately 1.0 s (see Fig. 4.9). These numbers are calculated for events that passed the whole fitting chain.

The final parameters for the prefit are given here:

- FilteringFit
  - InputHits: L1 hits
  - NumIterations: $10 \cdot 10^3$
  - $t_{\text{extra}} = 5\,\text{ns}$
  - $d_{\text{max}} = 300\,\text{m}$
  - $w = 0.5$
  - Minimum Cluster Size $N_{\text{hits}} \geq 6$

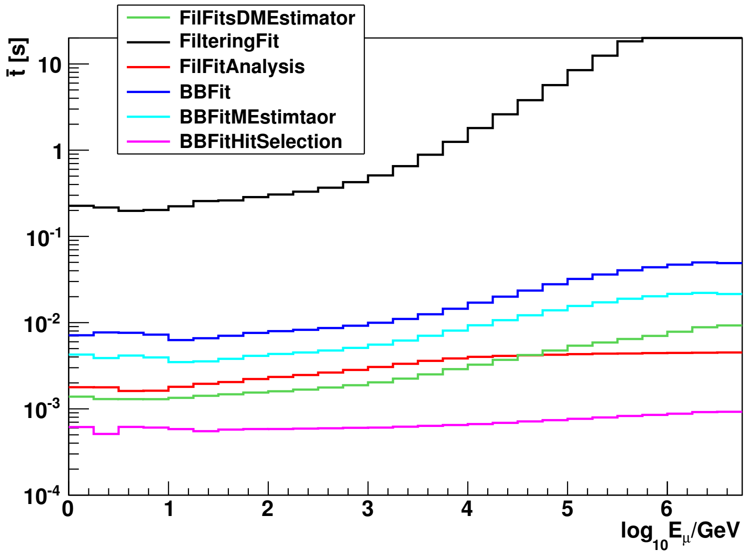

Figure 4.9: Mean computing time per event as a function of the muon energy. Only events were considered that passed the whole fitting chain.

  - $n = 10$
  - MinAngularDistanceForNewBestPoint $= 1°$

- FilteringFitsDTrackSelection
  - InputHits: L1 hits
  - InputTracks: 10 best FilteringFit tracks
  - HitSelection: $-5\,\text{ns} \leq t_{\text{res}} \leq 20\,\text{ns}$
- MEstimatorFit
  - InputHits: L0 hits
  - InputTrack: FilteringFitsD track
  - HitSelection: $-150\,\text{ns} \leq t_{\text{res}} \leq 150\,\text{ns}$, $d_{\text{max}} = 100\,\text{m}$

All steps up to now constitute a prefit, so a good approximation for the neutrino direction but not for the purpose of a point source search where a resolution of less then 1° is needed. Therefore a maximum-likelihood-based final fit is used to establish an high-resolution track reconstruction strategy. The idea is to find that trajectory that maximizes the likelihood for the given hit pattern $L = \prod_{i=1}^{N_{\text{hits}}} P_i(x_1, x_2, ...)$ or minimize the negative logarithm of it

$$-\log L = -\log \prod_{i=1}^{N_{\text{hits}}} P_i(x_1, x_2, ...) = -\sum_{i=1}^{N_{\text{hits}}} \log P_i(x_1, x_2, ...), \tag{4.15}$$

where $(x_1, x_2, ...)$ are the parameters of the probability function. The better the fit is the higher the likelihood should be and therefore the smaller the minus log-likelihood should be. So an quality parameter, if the fit converges well, is the reduced log-likelihood value (rlogL), which is

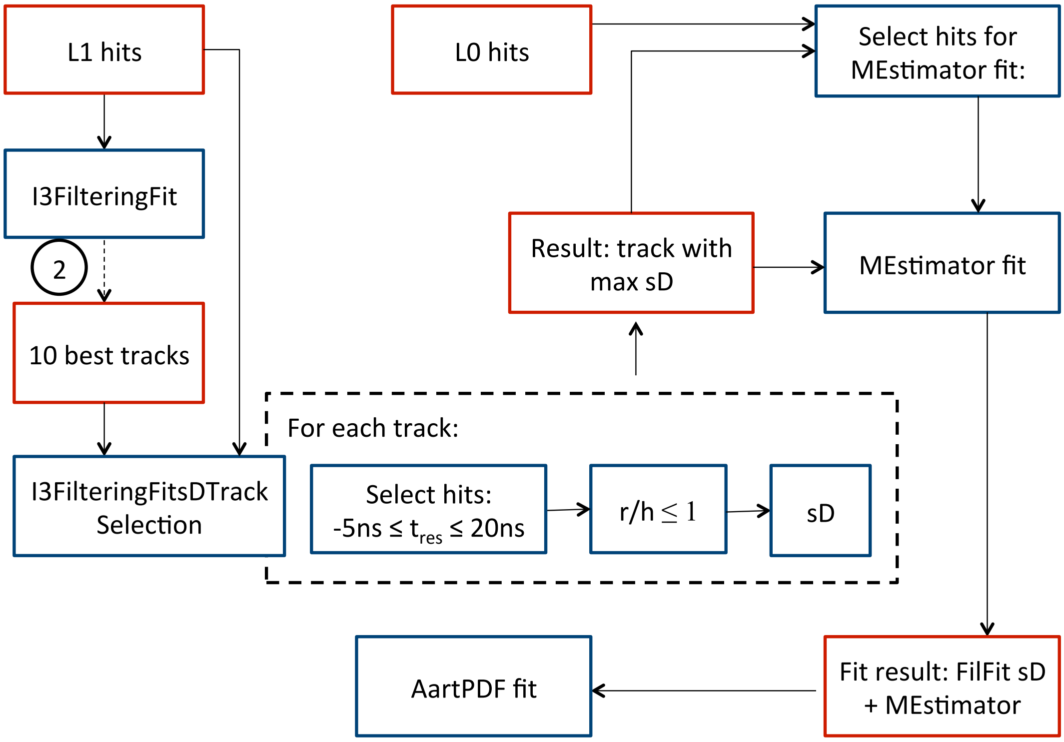

Figure 4.10: Overview of the enhancement of the FilteringFit track reconstruction chain (called 'FilteringFitsDMEstimator'). With the AartPDF fit as final fit it is called 'KrakeFit'. The '2' marks the optional path shown in Fig. 4.1. The cylinder criterion r/h and the surface density criterion sD is explained in section 4.2.2.

defined as rlogL = $\frac{\log L}{NDoF}$. Here the probability density function AartPDF developed in [34] was used, where the underlying hit time probability was extracted from simulations. For the final fit step an hit selection starting with all detected hits of the event (L0 hits) is performed, where hits are selected with small time residuals and small distances due to the FilteringFitsDMEstimator track. The maximal allowed distance of hits to the track is set to 300 m and the time residual limits are set to $t_{\text{res,min}} = -150$ ns and $t_{\text{res,max}} = 150$ns. Only the timing information and the position of the hits are used, their charge is not taken into account.

The whole fitting chain is called KrakeFit in the following. Its performance as compared to the standard ANTARES track reconstruction chains is studied in the following section.

4.3 Performance of KrakeFit

For the performance study $8 \cdot 10^{11}$ upgoing (anti-)neutrino events that were either triggered by the ANTARES 3N and/or 2T3 trigger algorithms ([42], [43], [44]) were used. In the following an optical background rate of 60 kHz random noise and a fully working detector were chosen if

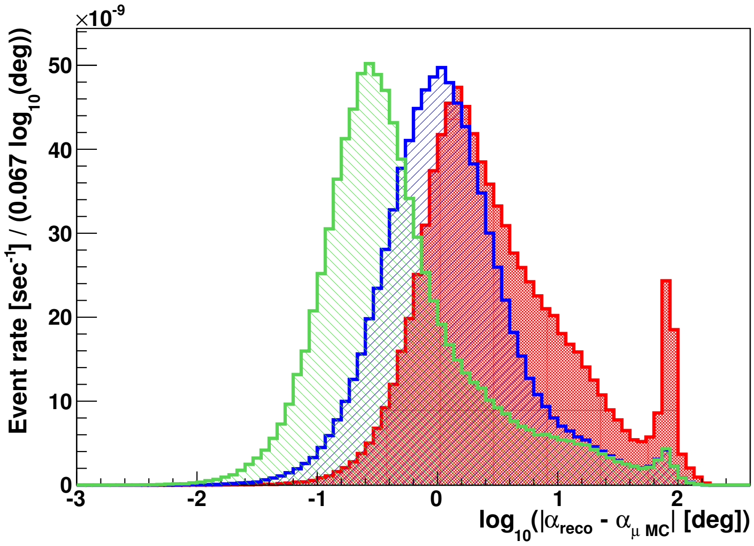

Figure 4.11: Distribution of the angular error $\Delta\alpha$ for the default output of FilteringFit (red), the result of the FilteringFitsDMEstimator (blue) and the KrakeFit result (green) with the cuts rdf=1, $s > 0.9$, rlogL < 5.6 for events reconstructed as upgoing. Events are weighted according to an E^{-2} spectrum.

not stated otherwise. The neutrinos have energies in the range between 10 GeV and 10 PeV and the events are weighted according to an E^{-2} spectrum. For the study of atmospheric muons the same detector conditions and trigger conditions were applied. Atmospheric muons are simulated corresponding to a live-time of 30 days with the parametrization of the muon flux described in [46].

The distribution of the angular error of the KrakeFit track reconstruction steps is shown in Fig. 4.11 for a combination of cuts obtained in section 4.3.1. To compare the results with other track reconstruction strategies it is important that the rate of misreconstructed atmospheric muons is nearly the same. Therefore an optimization of the cut parameters is done with respect to the rate of misreconstructed atmospheric muons.

4.3.1 Cut optimization

The reduced log-likelihood value of the final fit can be used as quality criterion of the fit. This value can also be used to distinguish between misreconstructed atmospheric muons and upgoing neutrinos which is shown in Fig. 4.12, where the cumulative distribution of rlogL is shown for upgoing reconstructed atmospheric neutrinos (dashed black curve) and misreconstructed atmospheric muons (continuous black curve). To get a reasonable misreconstruction rate of atmospheric muons a cut on rlogL < 5.5 is needed. So the question is, is it possible to use another parameter or value in order to get more neutrinos but the same misreconstruction rate? For this purpose an up-down-classification tool using random decision forest [47] is examined.

The use of the random decision forest (rdf) [47] is to identify upgoing events with high purity and high efficiency. The tool is available as the SeaTray module 'I3RDFClassify' [48]. In principle it has input parameters with several decision trees built on them that decide if the

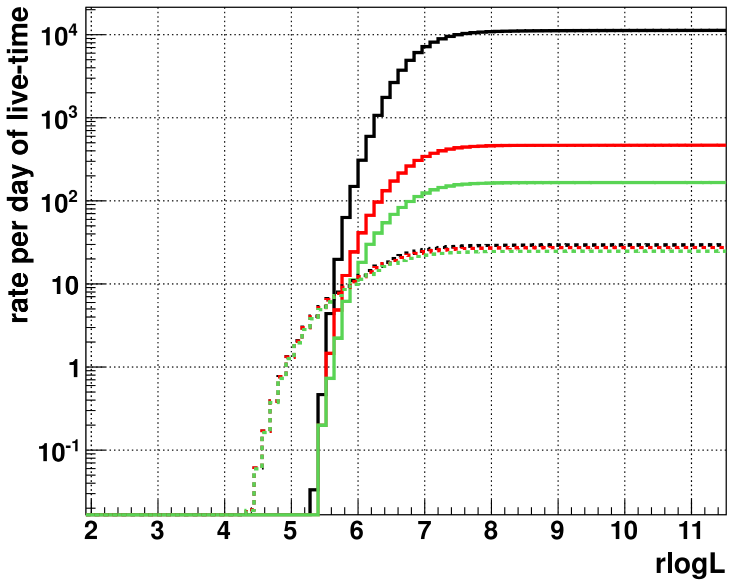

Figure 4.12: Cumulative distribution of the event rate per day of live-time depending on rlogL for upward reconstructed events with KrakeFit. Solid lines for atmospheric muons, dashed lines for atmospheric (anti-)neutrinos. The colors identify the cuts: black without cuts, red with rdf=1 and $s > 0.8$ and green rdf=1 and $s > 0.9$.

event is up- or down-going. The final decision is defined as the class where more than 50% of the decision trees agree. This is stored in the RDFClass (rdf) value which indicates if it is upgoing (rdf=1) or downgoing (rdf=0). Additionally the RDFSafety (s) value is stored which is the fraction of the trees which gave this decision. The higher this RDFSafety is, the more certain is the classification. Fig. 4.12 shows also the effect of the usage of rdf for two different safety (s) values, where the cumulative distribution of rlogL is shown for upward reconstructed events with KrakeFit (continuous lines for atmospheric muons, dashed lines for atmospheric neutrinos). From this plot one can see the effect of the rdf compared to the line without cut by looking at the rlogL value of 10, where the cumulative distribution is flat. The usage of rdf with $s > 0.8$ reduces the number of misreconstructed atmospheric muons by a factor of 22.4 and with $s > 0.9$ by a factor of 62.2. The number of upgoing reconstructed neutrinos is only slightly reduced, 93.4% (85.1%) of the neutrinos remain for rdf=1 with $s > 0.8$ ($s > 0.9$).

Another question is: does the rdf cut affect the performance of KrakeFit? As it shall only be used to distinguish between misreconstructed atmospheric muons and upgoing neutrinos it should not affect the resolution of the fit for neutrinos or the efficiency. A comparison is performed for neutrinos with an E^{-2} energy spectrum for KrakeFit without cut (blue line) and with rdf=1 and $s > 0.8$ (green line), which is shown in Fig. 4.13. By comparing the blue and the green curve in the upper left plot, one can see that the efficiency is slightly reduced for neutrino energies above 1 TeV, the difference of the efficiency for these curves is 1.3% (1.8%) for 1 TeV (100 TeV). The median of the angular error (lower left plot) for 1 TeV (100 TeV) is about 0.54° (0.18°) smaller. In the upper right plot the efficiency depending on the zenith angle is shown,